Monthly Notices of the ROYAL ASTRONOMICAL SOCIETY

MNRAS **515,** 3911–3937 (2022) https://doi.org/10.1093/mnras/stac1494
Advance Access publication 2022 June 7

PASSAGES: the Large Millimeter Telescope and ALMA observations of extremely luminous high-redshift galaxies identified by the Planck

Derek A. Berman,[1,2] Min S. Yun ,[1★] K. C. Harrington,[3] P. Kamieneski ,[1] J. Lowenthal,[4] B. L. Frye,[5] Q. D. Wang ,[1] G. W. Wilson,[1] I. Aretxaga,[6] M. Chavez ,[6] R. Cybulski,[1] V. De la Luz,[7] N. Erickson,[1] D. Ferrusca,[6] D. H. Hughes,[6] A. Montaña ,[6,8] G. Narayanan,[1] D. Sánchez-Argüelles,[6] F. P. Schloerb,[1] K. Souccar,[1] E. Terlevich,[6] R. Terlevich [6,9] and J. A. Zavala [10]

[1]*Department of Astronomy, University of Massachusetts, Amherst, MA 01003, USA*
[2]*Department of Earth and Atmospheric Sciences, Cornell University, Ithaca, NY 14853, USA*
[3]*European Southern Observatory, Alonso de Córdova 3107, Vitacura, Casilla 19001, Santiago de Chile, Chile*
[4]*Smith College, Northampton, MA 01063, USA*
[5]*Department of Astronomy/Steward Observatory, University of Arizona, 933 North Cherry Avenue, Tucson, AZ 85721, USA*
[6]*Instituto Nacional de Astrofísica, Óptica y Electrónica, Tonantzintla, 72000 Puebla, México*
[7]*Escuela Nacional de Estudios Superiores Unidad Morelia, Universidad Nacional Autónoma de México, Morelia, 58190, México*
[8]*CONACYT Research Fellow - SCiESMEX, Instituto de Geofísica, Unidad Michoacán, Universidad Nacional Autónoma de México, Morelia, Michoacán, México CP 58190, México*
[9]*Institute of Astronomy, University of Cambridge, Madingley Road, Cambridge CB3 0HA, UK*
[10]*National Astronomical Observatory of Japan, 2-21-1 Osawa, Mitaka, Tokyo 181-8588, Japan*

Accepted 2022 May 24. Received 2022 May 19; in original form 2021 April 9

ABSTRACT

The *Planck* All-Sky Survey to Analyze Gravitationally-lensed Extreme Starbursts project aims to identify a population of extremely luminous galaxies using the *Planck* all-sky survey and to explore the nature of their gas fuelling, induced starburst, and the resulting feedback that shape their evolution. Here, we report the identification of 22 high-redshift luminous dusty star-forming galaxies (DSFGs) at $z = 1.1$–3.3 drawn from a candidate list constructed using the *Planck* Catalogue of Compact Sources and Wide-field Infrared Survey Explorer all-sky survey. They are confirmed through follow-up dust continuum imaging and CO spectroscopy using AzTEC and the Redshift Search Receiver on the *Large Millimeter Telescope Alfonso Serrano*. Their *apparent* infrared luminosities span $(0.1–3.1) \times 10^{14}$ $L_\odot$ (median of 1.2×10^{14} $L_\odot$), making them some of the most luminous galaxies found so far. They are also some of the rarest objects in the sky with a source density of $\lesssim 0.01$ deg^{-2}. Our Atacama Large Millimeter/submillimeter Array 1.1 mm continuum observations with $\theta \approx 0.4$ arcsec resolution show clear ring or arc morphologies characteristic of strong lensing. Their lensing-corrected luminosity of $L_{\rm IR} \gtrsim 10^{13}$ $L_\odot$ (star-formation rate $\gtrsim 10^3$ $M_\odot$ yr^{-1}) indicates that they are the magnified versions of the most intrinsically luminous DSFGs found at these redshifts. Our spectral energy distribution analysis finds little detectable active galactic nucleus (AGN) activity despite their enormous luminosity, and any AGN activity present must be extremely heavily obscured.

Key words: galaxies: high-redshift – galaxies: ISM – galaxies: starburst – gravitational lensing: strong – infrared: galaxies – submillimetre: galaxies.

1 INTRODUCTION

An important unanswered question in our understanding of the cosmic star-formation (SF) history is how a large quantity of cold gas is continuously and rapidly funnelled into the central 1–10 kpc regions of dark matter haloes to form 10^{11} $M_\odot$ or more of stars over just a few hundred million years, only 2–3 billion yr after the big bang. A related question is how this flow is regulated so that the stellar mass growth is shut off just at the right moment so that theoretical predictions and observational data on mass functions are in agreement at both high- and low-mass ends. Observations have shown that the bulk of the stellar mass build-up during the peak of the cosmic SF density at $z \approx 2$–4 ('cosmic noon') has occurred in massive galaxies with star-formation rate (SFR) of 10s to 100s of solar masses per year with a characteristic gas depletion time of only $\sim 10^8$ yr (see Casey, Narayanan & Cooray 2014; Madau & Dickinson 2014). Their apparent local analogues, luminous infrared galaxies (LIRGs) and ultraluminous infrared galaxies (ULIRGs) with a similarly high SFR and gas depletion time, are rare in the current epoch, and their large gas inflow rates are associated with strong tidal disruptions and major mergers (see the review by Sanders & Mirabel 1996). Strong tidal disruptions and mergers were likely important in early epochs as well, but the average gas accretion rate was also generally much higher in earlier epochs because mean gas mass density was higher. The extremely luminous starburst

★ E-mail: myun@astro.umass.edu

© 2022 The Author(s)
Published by Oxford University Press on behalf of Royal Astronomical Society

Downloaded from https://academic.oup.com/mnras/article/515/3/3911/6603847 by guest on 28 January 2026

galaxies with $L_{\rm IR} \gtrsim 10^{12–13}$ $L_\odot$ ($SFR \gtrsim 100–1000$ $M_\odot$ yr^{-1}) discovered by submillimetre and far-infrared (FIR) wavelength surveys ('submillimetre galaxies' or SMGs; see reviews by Blain et al. 2002; Casey et al. 2014) have no counterparts in the local universe. Their extreme luminosity requires an uncertain extrapolation of our current knowledge on gas inflow, and an entirely different process might be at work.

One way to gain new insight into the gas inflow powering this rapid galaxy growth is to identify a population with the most extreme luminosity. The maximal gas accretion associated with these objects might offer a way to discriminate among different competing processes. The key feedback processes that regulate the galaxy growth, either radiative or mechanical, are also likely operating maximally at the same time, making them excellent laboratories for studying the nature and efficiency of the feedback processes as well. The main aim of our *Planck* All-Sky Survey to Analyze Gravitationally-lensed Extreme Starbursts (PASSAGES) project is to identify a population of the most luminous galaxies using the *Planck* all-sky survey and to explore the nature of the gas inflow, its induced starburst, and the resulting feedback and its impact. As described below, nearly all of the objects we have identified are strongly magnified by gravitational lensing, and they also offer an exceptional opportunity to probe the relevant physical processes on spatial scales of 100 pc or better, which is normally beyond the reach of the existing astronomical facilities (0.1 arcsec $\approx$ 1 kpc at $z > 1$).

A systematic search for high-redshift objects hosting an extremely luminous starburst and/or a supermassive black hole (SMBH) should be most productive in the infrared (IR) wavelengths, as they are expected to be heavily dust-obscured. Considering the expected trend of decreasing *mean* metallicity with look-back time, this is not an obvious choice. However, Cen & Ostriker (1999) and others have shown that metallicity evolution is driven by local density, rather than by cosmic time, and the highest density regions quickly approach near-solar metallicity even at high redshifts. This theoretical prediction is now supported by a growing list of systematic observational studies. By analysing the 3D-HST treasury programme and the CANDELS data, Whitaker et al. (2017) found a strong dependence of the fraction of obscured SF on stellar mass, with remarkably little evolution with redshift out to $z = 2.5$, with over 50 and 90 per cent of SF being obscured at $\log(M_*/M_\odot) = 9.4$ and 10.5, respectively. Deshmukh et al. (2018) and others have shown that the importance of dust-obscured SF activity extends to $z \approx 6$. Among the submillimetre-selected high-redshift galaxies to $z \sim 4$ and beyond, objects with little or no detectable optical/near-IR emission in even the deepest *Hubble Space Telescope (HST)* exposures are common, presumably because of extinction and the red colour of their stellar hosts (Wang, Barger & Cowie 2009; Yun et al. 2012; Wang et al. 2016; Yamaguchi et al. 2019; Smail et al. 2021).

Prior to the analysis of the compact sources identified by the *Planck* all-sky multiwavelength surveys, the most luminous high-redshift population of objects identified through a *systematic* study were the hyperluminous infrared galaxies (HyLIRGs) identified by the all-sky Wide-field Infrared Survey Explorer (*WISE*) survey (Tsai et al. 2015). A sampling of compact sources identified in the *Planck* all-sky survey using the *Herschel* Space Observatory has yielded some of the most luminous galaxies identified thus far (Cañameras et al. 2015; Harrington et al. 2016), with most of their luminosity seen in the rest frame IR.[1] Wide-area cosmic microwave background surveys at millimetre wavelengths, such as by the *South Pole Telescope* (*SPT*; Carlstrom et al. 2011) and the *Atacama Cosmology Telescope* (*ACT*; Fowler et al. 2007), have also yielded a population of strongly lensed high-redshift dusty star-forming galaxies (DSFGs) that are less luminous but at higher redshifts to $z \gtrsim 6$ (Greve et al. 2012; Marsden et al. 2014; Spilker et al. 2016; Su et al. 2017; Gralla et al. 2020).

In this paper, we report the identification of 22 luminous high-redshift sources at $z = 1.1–3.3$ with apparent IR luminosity of $L_{\rm IR} \geq 10^{13–14}$ $L_\odot$ selected from the *Planck* Catalogue of Compact Sources (PCCS; Planck Collaboration XXVIII 2014) and confirmed using the AzTEC 1.1 mm continuum imaging and CO spectroscopy obtained using the Redshift Search Receiver (RSR) on the *Large Millimeter Telescope (LMT)*. We also report Atacama Large Millimeter/submillimeter Array (ALMA) 1.1 mm continuum imaging and photometry of a subset of 12 sources obtained at $\theta \sim 0.4$ arcsec resolution to confirm that all of these sources are strongly lensed high-redshift DSFGs. We first describe how the high-redshift candidates are identified from the parent PCCS catalogue using *WISE* photometry. Their confirmation as high-redshift sources using the follow-up *LMT* and ALMA follow-up observations is described in Section 3, and the characterization of their spectral energy distribution (SED) and apparent IR luminosity is discussed in Section 4. Finally, the physical origin of their enormous luminosity is explored by examining the evidence for luminous active galactic nucleus (AGN) and gravitational lensing, as well as the gas content and gas consumption time, in Section 5.

2 IDENTIFICATION OF PLANCK HIGH-REDSHIFT CANDIDATES

One of the data products the *Planck* collaboration has published as part of their general data release is the PCCS, which is a set of single-frequency catalogues of Galactic and extragalactic compact sources covering the entire sky in the frequency range 30–857 GHz. Following the first release catalogue based on the initial 15 months of mission (PCCS1, Planck Collaboration XXVIII 2014), the second release catalogue including the full survey was released in 2015. The second data release (DR2) consists of two subcatalogues: the PCCS2 (4891 & 1694 sources in the 857 & 545 GHz bands, respectively) with known reliability and the larger PCCS2E (43290 & 31068 sources in the 857 & 545 GHz bands, respectively, mostly within the Galactic mask) with 'unknown reliability' (Planck Collaboration XXVI 2016).[2] Both *Planck* compact source catalogues are heavily confusion limited so that the flux density and the reliability of each catalogue entry are limited by its location on the sky and data-reduction methods, rather than by thermal noise. The PCCS2 is deemed more reliable and thus supersedes the PCCS1, but we found it useful to examine both catalogues since we are exploring the faintest sources in each catalogue where the catalogue completeness is poor.

When we started this project, only the PCCS1 was available, and we developed and built the high-redshift source identification technique using the PCCS1 only. When the PCCS2 and PCCS2E became available, we applied the same technique developed earlier and found similar results but also with some notable differences. One of the key limitations we encountered with both the PCCS1 & the

[1] While *Herschel* surveys have been extremely successful in finding thousands of high-redshift DSFGs, their limited survey coverages (less than 10 per cent of the sky) have led to only a handful of $L_{\rm IR} \gtrsim 10^{14}$ $L_\odot$ sources – see Harrington et al. (2016).

[2] See Planck Collaboration LV (2020) for more detailed discussions of the reliability of the PCCS2 sources.

Downloaded from https://academic.oup.com/mnras/article/515/3/3911/6603847 by guest on 28 January 2026

PCCS2 is that the photometry for a given high-redshift candidate source is frequently incomplete for the full set of frequency bands. The PCCS catalogues are published by the *Planck* project for each frequency band separately, and we had to create a band-merged catalogue ourselves through position matching. Because these candidate high-redshift sources are typically among the faintest sources near the reliability limit, missing a flux density entry in one or more bands in our band-merged catalogue is not uncommon. This is an important limitation because any sources with missing photometry in the critical high frequency bands have to be excluded in our selection method, which is based on a colour–magnitude filter (see below for further discussions). In the end, we constructed our master band-merged photometry catalogue using primarily the PCCS2 and filling in any missing photometry from the PCCS1 if possible. This band-merged catalogue is used in the subsequent filtering of the data to identify the candidate high-redshift *Planck* sources.

We note that the *Planck* collaboration has published its own *Planck* High-redshift Source Catalogue (PHZ; Planck Collaboration XXXIX 2016) using a different source identification and photometric and colour analysis. We find a surprisingly small overlap between the PHZ and our own high-redshift candidate catalogue, and we discuss this further in Section 5.

2.1 Filtering the Planck catalogues

The majority of the sources in the PCCS catalogues are expected to be radio AGNs (including blazars) in the 217 GHz and lower frequency bands and star-forming galaxies (SFGs) and Galactic cirrus in the 353 GHz and high-frequency bands (Planck Collaboration VII 2013; Planck Collaboration XXVIII 2014). To identify high-redshift DSFGs, we construct a set of filters that will remove foreground Galactic cirrus sources with $T_{\rm d} \approx 20$ K and radio AGNs. The former is accomplished by adopting the Galactic Foreground filter established by the Planck collaboration. Removing radio AGNs is achieved by constructing a classic 'colour–magnitude' filter that exploits the distinct shape differences between thermal dust emission and power-law non-thermal AGN SEDs. The main ideas behind these filters are fairly simple and intuitive, and they are nearly the same as those described by Planck Collaboration XXXIX (2016). An important difference in our approach is that we kept the filtering simpler so as to minimize the negative impact of relatively low signal-to-noise ratio (SNR) in the photometry and to prevent introducing too many assumptions and potential biases. Instead, we exploit the wealth of multiwavelength data available to refine the selection of high-redshift galaxy candidates and ultimately to prioritize the targets for follow-up observations using the *LMT* (see Section 3). The flow of the data through this filtering process is summarized as a diagram in Fig. 1, and the key steps are explained in greater detail below.

2.1.1 Galactic foreground mask

The removal of foreground Galactic cirrus sources is accomplished primarily by excluding sources in the directions of the Galactic plane and known filamentary Galactic foreground structures. Specifically, this is accomplished by: (i) applying a Galactic latitude limit of 30 degrees (i.e. $|b| \geq 30^{\circ}$); and (ii) excluding all sources falling within the Galactic zone and filament masks[3] derived by the *Planck* team using neutral hydrogen column density (see Planck Collaboration XI 2014, for further details). The Galactic mask we adopted is essentially the same as the one adopted by the *Planck* team for their high-redshift source candidate identification (see the fig. 1 by Planck Collaboration XXXIX 2016), except our coverage is slightly larger since we are not bound by the *Infrared Astronomical Satellite (IRAS)* survey coverage. The resulting total sky coverage for our high-redshift galaxy search is 27.9 per cent or 11 500 square degree in area.

The total number of sources remaining after the Galactic mask is applied to the 857 GHz based band-merged catalogue is 4825, 3965, and 1827 sources for the PCCS1, the PCCS2, and the PCCS2E, respectively (see Table 1). The fraction of the PCCS1 sources found outside the Galactic mask is only 20 per cent, suggesting that a large majority of the 857 GHz-selected sources are associated with Galactic structure. This is also obvious in the source distribution shown in fig. 2 by Planck Collaboration XXVI (2016). The total combined number of 857 GHz sources in the PCCS2 and PCCS2E is nearly twice as large as in the PCCS1, but the number outside the Galactic mask region increases only by 20 per cent. Therefore, most of the new sources identified in the DR2 catalogues are within the Galactic mask region.

The situation is similar in the 545 GHz band in that the total number of sources is doubled in the DR2 compared to DR1, but the increase outside the Galactic mask region is almost negligible (1 per cent). The fraction of sources outside the Galactic mask region is much smaller, 1064/16933 = 6.3 per cent and (403+672)/(1694 + 31068) = 3.3 per cent for the DR1 and the DR2 catalogues. The total number of 545 GHz band-merged catalogue sources that are undetected in the 857 GHz band remains virtually the same between the two data releases. It is also interesting that the fraction of 'highly reliable' 545 GHz band sources in the PCCS2 catalogue drops to only 24 per cent of the total outside the Galactic mask region, in contrast to the 857 GHz band (75 per cent). This illustrates the complex way the foreground confusion plays an important role in shaping these *Planck* compact source catalogues.

2.1.2 Selection by SED and apparent IR luminosity

The intrinsic SED of DSFGs is characterized by a prominent dust peak with average dust temperature of $T_{\rm d} \approx 30$–40 K (see the review by Casey et al. 2014). The observed dust peak shifts to a longer wavelength with increasing redshift with apparent characteristic temperature of $T_{\rm d}/(1+z)$ as shown in Fig. 2. As a consequence, the peak of the dust SED shifts through the three highest frequency *Planck* bands at $z \approx 1.5$, $z \approx 2.5$, and $z \approx 4$, respectively. In contrast, the Galactic cirrus emission with $T_{\rm d} \approx 15$–25 K peaks at a much shorter wavelength, around $\lambda \approx 100-150\,\mu$m, and this difference in SED can be an important discriminator between high-redshift DSFGs and Galactic cirrus sources.

Another potentially important discriminator is the measured flux density in these *Planck* bands. The DSFG SED template with a SFR of $SFR = 344$ M$_{\odot}$ yr^{-1} by Kirkpatrick et al. (2012) predicts flux densities of ∼50 and ∼30 mJy in the *Planck* 857 and 545 GHz bands at $z = 1$ and less than 20 mJy in both bands at $z \geq 2$ (see Fig. 2). Since the flux density sensitivity for these bands in the PCCS1 and the PCCS2 is ∼100 mJy, only the DSFGs with apparent $SFR \gtrsim 1000$ M$_{\odot}$ yr^{-1} can be detected by *Planck* at $z \lesssim 1.5$. At $z \geq 2$, detection by *Planck* would require $SFR \geq 2000$ M$_{\odot}$ yr^{-1}, which is near the upper bound of the most active SFGs discovered previously (e.g. Yun et al. 2012, 2015). The predicted flux density falls rapidly in the longer wavelength bands as $S \propto \lambda^{-3.5}$, making a detection much less likely in the 353 GHz and lower frequency bands.

[3] https://irsa.ipac.caltech.edu/data/Planck/release_2/ancillary-data/

Downloaded from https://academic.oup.com/mnras/article/515/3/3911/6603847 by guest on 28 January 2026

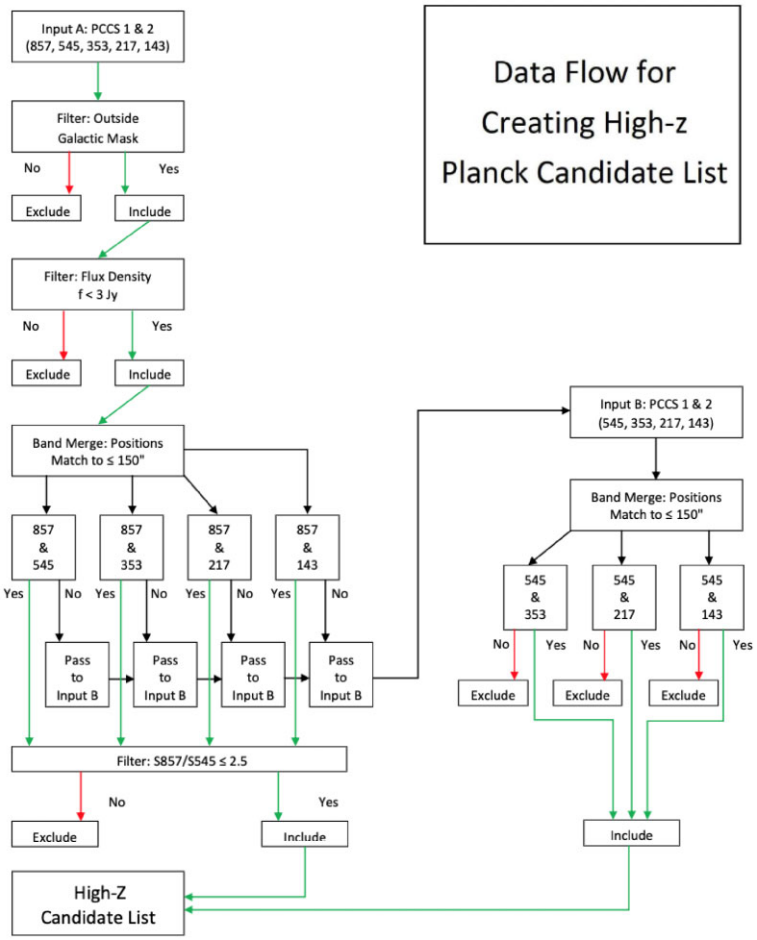

Figure 1. A data flow diagram for creating the final *Planck* high-redshift candidate list from the PCCS1 and PCCS2 catalogues. The second pass through the colour–magnitude filter on the right side of the diagram is for the higher redshift ($z \gtrsim 3$) sources whose dust peak is shifted out of the 857 GHz band and thus are undetected in that band.

Table 1. Summary of *Planck* catalogue filtering.

Frequency	Total	Mask only	Mask + filter
857 GHz band:			
PCCS1	24 381	4825	311
PCCS2	4896	3965	218
PCCS2E	43 290	1827	97
545 GHz band:			
PCCS1	16 933	1064	111
PCCS2	1694	403	112
PCCS2E	31 068	672	19

Our high-redshift DSFG selection algorithm is illustrated on the left-hand panel of Fig. 3. Since the great majority of sources in the PCCS catalogues are foreground Galactic cirrus sources, our primary aim here is to exclude as many of the Galactic dust clumps as possible by: (i) excluding sources with a high flux density ratio between the 857 and the 545 GHz band (i.e. $S_{857\mathrm{GHz}}/S_{545\mathrm{GHz}} \geq 2.5$) and (ii) also excluding all sources brighter than 3 Jy in the 857 GHz band. The first criterion is a simple and effective way to capture the SED differences illustrated in Fig. 2, while the second criterion excludes sources that are too bright to be extragalactic even in the presence of lensing (see below). The precise details of the selection criteria are somewhat arbitrary. The specific values adopted do change between independent studies, in each case resulting in a successful set of *Planck*- and *Herschel*-selected high-redshift sources (filled magenta points in Fig. 3).[4] Adopting the template SED for the average $z = 2$ DSFG by Kirkpatrick et al. (2012) shown in Fig. 2, the upper flux density limit of $S_{857\mathrm{GHz}} = 3$ Jy translates to a SFR of $SFR \approx 20\,000$ $\mathrm{M_\odot\,yr^{-1}}$ ($L_{\mathrm{IR}} \approx 10^{14.3}$ $\mathrm{L_\odot}$) at $z = 1$ and $SFR \gtrsim 70\,000$ $\mathrm{M_\odot\,yr^{-1}}$ ($L_{\mathrm{IR}} \approx 10^{14.9}$ $\mathrm{L_\odot}$) at $z \geq 2$. These SFRs are unusually large, explainable only with the aide of the largest lensing magnification ever seen, as discussed by Harrington et al. (2016). There is a limit to a plausible magnification factor for an extended object like a galaxy, which is rarely much larger than 20–30 (e.g. Bussmann et al. 2013, 2015; Spilker et al. 2016). Therefore, an apparent SFR of 30 000–60 000 $\mathrm{M_\odot\,yr^{-1}}$ is the upper bound of the most luminous FIR sources *Planck* might detect. The flux density limit we chose is twice as large as the brightest *Planck* high-redshift source discovered thus far, and it is seven times higher than the measured flux density[5] of the most luminous IR QSO known, APM

[4]The magenta points in Fig. 3 also include five additional *Planck* sources already known in the literature, as discussed in Section 2.5. They are not used in the definition of the colour–magnitude cuts since they are identified from the high-redshift candidate list produced by this study.

[5]$S_{350\mu} = 437 \pm 14$ mJy measured by the *Herschel* SPIRE instrument, from NASA/IPAC IRSA.

Downloaded from https://academic.oup.com/mnras/article/515/3/3911/6603847 by guest on 28 January 2026

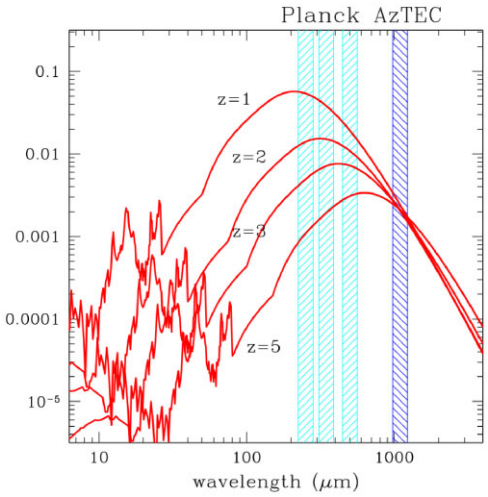

Figure 2. A model SED of a DSFG observed at a redshift of $z = 1$, 2, 3, and 5. The dust peak of a $z = 1$ SFG is located near $\lambda \approx 200$ μm, leading to a monotonic decrease in observed flux density in the 857 GHz band, to 545 GHz band, and then to 353 GHz band of the *Planck*. As a galaxy is observed at an increasingly higher redshift, the dust peak shifts to a longer wavelength. Exploiting this systematic trend is the basic idea behind our high-redshift source selection algorithm. The template SED shown is that of the average $z = 2$ SFG observed by *Herschel* and *Spitzer* with a derived SFR $SFR = 344$ $M_\odot$ yr^{-1} (Kirkpatrick et al. 2012). This figure illustrates how the flux density ratio of a DSFG flattens across the *Planck* and AzTEC bands with increasing redshift. The detection limit of *Planck* PCCS catalogues is about 300 mJy in 857 and 545 GHz (at the top edge of this plot), so an object must have an apparent $SFR \geq 3000$ $M_\odot$ yr^{-1} in order to make it into our sample.

08279+5255 (Irwin et al. 1998; Weiß et al. 2007) – see further discussions on possible dusty quasars in Section 5.1.1.

As the dust peak shifts out of the 857 GHz band and into the 545 GHz band at $z \approx 2$, the observed flux density in the 857 GHz band begins to fall rapidly with increasing redshift, as shown in Fig. 2, and $z \gtrsim 3$ DSFGs might drop out of the *Planck* 857 GHz band source catalogue entirely. Instead, these higher redshift sources would appear in the band-merged catalogue based on the *Planck* 545 GHz catalogue. Indeed four (out of 15) high-redshift *Planck* sources previously identified using the *Herschel* data are 857 GHz dropouts. As summarized in Table 1, the number of 545 GHz band-selected sources are far fewer than the 857 GHz detected sources, and the confirmed high-redshift *Planck* sources are much harder to identify by their flux density or by their S_{545GHz}/S_{353GHz} flux density ratio (see the right-hand panel of Fig. 3). Therefore, the entire 545 GHz-selected sources are passed along to the next step without any further filtering. The fact that they are undetected in the 857 GHz band immediately rules out their possible Galactic cirrus origin.

The net result of applying both the Galactic foreground mask and colour–magnitude filter to the *Planck* 857 GHz-selected sources is that a total of 311 and 315 high-redshift candidate sources are identified from the PCCS1 and PCCS2 catalogues, respectively (see the far-right column of Table 1). For the 545 GHz-selected sources without an 857 GHz band detection, a total of 111 and 131 high-redshift candidate are identified without any further colour or magnitude cut. The PCCS1 & PCCS2 high-redshift candidate lists largely overlap as expected, but there are also notable differences. Therefore, both lists are carried through for the remainder of the sample selection process in parallel.

The total number of high-redshift *Planck* source candidates we have identified here is much smaller than the total of 2151 high-redshift *Planck* source candidates identified in essentially the same area by the *Planck* project team using their own SED modelling (*Planck* Collaboration XXXIX 2016). This discrepancy arises from differences in the parent catalogues and data filtering, which we discuss in detail in Section 5.3.

2.1.3 Removal of nearby galaxies and radio AGNs

Although we are able to remove more than 98 per cent of likely foreground Galactic sources through the filtering described above, two important classes of contaminating sources remain: (i) nearby galaxies that are bright enough to be detected by *Planck*, and (ii) radio AGNs that are strongly beamed. A check on the coordinates revealed that a large number of the remaining *Planck* sources are in the direction of nearby galaxies such as the Large and Small Magellanic Clouds, M31, and M33. Some of the 545 GHz-selected sources are also well-known 3C radio sources and bright radio quasars and blazars.

We remove potentially contaminating nearby galaxies and radio AGNs by performing a cone search for any known extragalactic sources within the 2.5 arcmin radius *Planck* beam in the NASA Extragalactic Database (NED).[6] Specifically, we removed any *Planck* sources from our candidate list if one or more optically bright galaxies (typically a galaxy at $z \lesssim 0.1$ in the NGC or an IC catalogue) or a bright radio source [e.g. brighter than 20 mJy in the 1.4 GHz National Radio Astronomy Observatory Very Large Array sky survey (NVSS) or Faint Images of the Radio Sky at Twenty-Centimeters (FIRST) survey] is found in the NED cone search.

2.2 Identifying and prioritizing the optical and near-IR counterpart candidates

Identifying specific individual high-redshift DSFG or galaxies responsible for the submillimetre continuum emission is another highly challenging task. Each 2.5 arcmin radius *Planck* beam area includes ≈20 000 galaxies at the depth of the *HST* survey of the Hubble Ultra-Deep Field (Beckwith et al. 2006), and additional information is required to accomplish this task. Here, we utilize the *WISE* all-sky survey (Wright et al. 2010) to identify the likely optical and near-IR counterparts to our high-redshift DSFGs by exploiting their characteristic red SED in these wavelength bands.

High-redshift DSFGs at $z \geq 1$ are exceedingly faint and red in their rest frame ultraviolet (UV) bands, and their intense star-forming regions can be heavily obscured by dust (see Yun et al. 2008, 2012; Whitaker et al. 2017; Smail et al. 2021, and references therein). Yun et al. (2008) have shown that these galaxies have an extremely red UV to near-IR SED, characteristic of heavily obscured young stellar populations, and yet they are bright and are easily detected in their rest frame photospheric emission traced by the *Spitzer* 3.6 and 4.5 μm bands. The combined effects of their intrinsic red colours and a favourable *k*-correction make these high-redshift DSFGs easily distinguishable from the foreground population – see figs 12 and 13 of Yun et al. (2012). Unfortunately, the necessary *Spitzer* photometry is not available in most parts of the sky, and the *WISE* all-sky survey (Wright et al. 2010) offers the next best photometric data in the near-IR bands. Although significantly shallower and three times worse in angular resolution [∼6 arcsec full width at half-maximum (FWHM)]

[6] https://ned.ipac.caltech.edu

Downloaded from https://academic.oup.com/mnras/article/515/3/3911/6603847 by guest on 28 January 2026

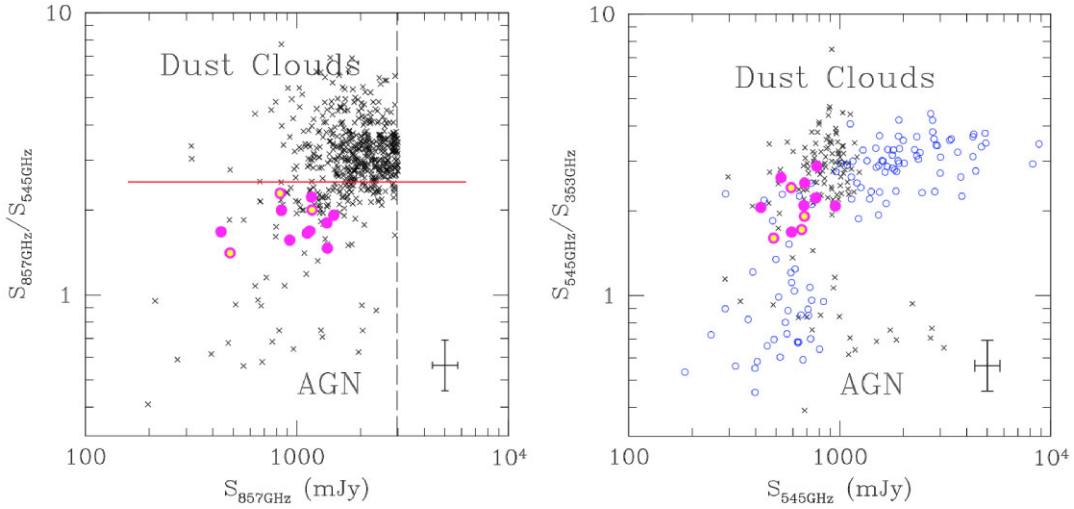

Figure 3. Plots of flux density ratios as a function of flux density for *Planck* PCCS sources. The flux ratios of S_{857GHz}/S_{545GHz} for the PCCS sources identified in the 857 GHz band are shown as small crosses on the left-hand panel. The flux density cutoff of $S_{857GHz} = 3$ Jy is shown with a vertical dashed line. The red horizontal line at $S_{857GHz}/S_{545GHz} \geq 3$ is used to exclude PCCS sources associated Galactic dust clouds (also low-z galaxies) from the flat spectrum radio AGNs and high-redshift dusty galaxies (filled magenta points, Herranz et al. 2013; Cañameras et al. 2015; Harrington et al. 2016, also see Section 2.5). A subsample from the *Planck–Herschel* study by Cañameras et al. (2015) is shown as magenta circles. The S_{545GHz}/S_{353GHz} ratios for the PCCS sources identified in the 545 GHz band are shown as small crosses on the right-hand panel, and all sources undetected in the 857 GHz band are shown as blue circles. Confirmed high-redshift sources (magenta dots) are on the bottom range of the S_{545GHz}/S_{353GHz} ratio for the dust sources. Almost all sources with $S_{545GHz}/S_{353GHz} \lesssim 2$ are known flat spectrum radio AGNs and blazars such as 3C 84, 3C 279, and 3C 454.3, with a characteristic flat spectrum of $S_{857GHz}/S_{545GHz} \lesssim 1$. Typical uncertainties for the photometry and flux ratio are shown on the bottom right corner of each figure.

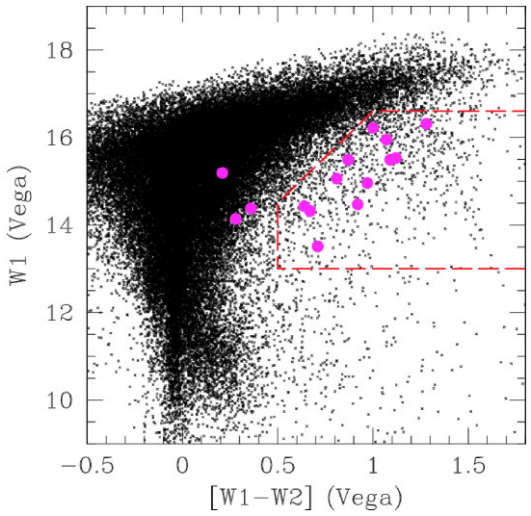

Figure 4. A colour–magnitude plot of *WISE* *W*1 (3.4 μm) and *W*2 (4.6 μm) photometry for the sources found in the *Planck* high-redshift candidate source fields. Large filled (magenta) circles are the 15 *Planck–Herschel* sources reported by Herranz et al. (2013), Cañameras et al. (2015), and Harrington et al. (2016), while the small dots show more than 50 000 *WISE* sources found within the 2.5 arcmin search radius from the *Planck* PCCS catalogue positions of the high-redshift candidate sources. A long dashed line marks the selection boundary for the area of candidate high-redshift sources – see the text for the details.

than the *Spitzer* IRAC data, the *WISE* all-sky survey is sensitive enough to detect the high-redshift *Planck* sources (see below and Section 4.3).

The near-IR colour–magnitude filter we adopted for separating DSFGs at $z \geq 1$ from the foreground galaxy population is shown in Fig. 4. The basic principle behind this filter is to identify and exclude *WISE* sources that are too blue and too bright to be $z \gtrsim 1$ DSFGs, with a magnitude cutoff to exclude all low-SNR sources in the *WISE* catalogue. As was first shown by Wright et al. (2010), nearly all of the nearby galaxies have the characteristic *WISE* colours of $[W1 - W2] \approx 0.0$ in Vega magnitudes because their light is dominated by stellar photospheric emission. Our colour selection of $[W1 - W2] \geq 0.5$ effectively removes all but the most dust obscured galaxies and AGNs (Wright et al. 2010). The lower magnitude cutoff of $W1 \leq 16.6$ is the 5σ completeness limit of the *WISE* all-sky source catalogue,[7] and a diagonal wedge between $(W1, W2) = (+0.5, +14.5)$ and $(W1, W2) = (+1.0, +16.6)$ was added to mitigate the impact of the noisier *W*2 band photometry (5σ completeness limit of $W2 \leq 15.5$). Lastly, a bright end magnitude cutoff of $W1 \geq 13.0$ is added as an empirical filter to exclude galaxies that are too bright to be at $z \geq 1$ (see below). This bright end cutoff was designed to remove any confusing bright foreground galaxies, but it is still not restrictive enough to remove any of the *WISE*-selected HyLIRGs reported by Tsai et al. (2015), which is important in our IR AGN discussion (see Section 5.1.1).

A direct outcome from this *WISE* colour–magnitude filtering is that the individual galaxies likely responsible for the *Planck* detection are identified with one arcsec positional accuracy. With this localization, these *WISE*-selected *Planck* sources (‘*Planck–WISE* sources’ hereafter) can now be examined further through targeted follow-up observations and SED analysis.

The effectiveness of this colour–magnitude filter and the impact of a possible foreground confusion are tested by examining those of the *Herschel*-selected *Planck* sources, shown as large filled circles in Fig. 4. A total of 12 (out of 15) *Herschel*-selected sources fall within the selection filter area while three sources fall within the foreground galaxy cloud. Essentially *all* of these sources are high-redshift DSFGs magnified by a foreground lensing galaxy or a galaxy

[7] http://wise2.ipac.caltech.edu/docs/release/allsky/

Downloaded from https://academic.oup.com/mnras/article/515/3/3911/6603847 by guest on 28 January 2026

group, but the lensed DSFGs dominate the combined photometry and yield the characteristic extreme red colour in most cases. For the three sources outside the selection region, the foreground lensing galaxies are brighter than the lensed DSFGs, shifting them outside the selection region. This represents the primary mode by which our *WISE* colour–magnitude filter might exclude otherwise good high-redshift DSFG candidates. This *Herschel*-selected *Planck* sample is entirely independent of *WISE* data, and therefore a loss of ∼20 per cent of high-redshift galaxy candidates from this analysis is a reasonable estimate for our colour–magnitude filter. We note that Iglesias-Groth et al. (2017) developed a similar near-IR colour selection method for high-redshift DSFGs, and Díaz-Sánchez et al. (2017) used this method to discover independently one of our sources PJ132934.2 as a strongly lensed high-redshift DSFG without any *Planck* prior (see the discussion in Appendix B).

2.3 Sample statistics and completeness

After removing all high-redshift *Planck* source candidates associated with nearby galaxies and radio AGNs (Section 2.1.3) and applying our *WISE* band colour–magnitude filter, the final list of likely *Planck* sources associated with a high-redshift DSFG includes 118 *WISE* sources. This corresponds to a mean source density of 10^{-2} per square degree, which is smaller than that of the strongly lensed high-redshift DSFGs found by *Herschel* (0.02–0.1 per square degree; Vieira et al. 2013; Wardlow et al. 2013; Weiß et al. 2013) and is among the rarest population of extragalactic sources known. Here, we report the AzTEC 1100 μm photometry and CO spectroscopy of the confirmed high-redshift sources so far. The entire candidate source catalogue and follow-up observations will be published elsewhere when the *LMT* follow-up observations are completed.

The main shortcoming of using the *Planck* data is the severe confusion noise associated with its large survey beam size. While all PCCS sources are highly statistically robust ($\geq 7\sigma$), the PCCS photometry carries a large systematic uncertainty (see Table 3). This means the completeness of the sample depends on the foreground and background confusion, and this is the leading limitation for the sample. Follow-up studies using *Herschel* and other telescopes have shown that extragalactic PCCS sources are mixes of bright individual sources as well as groups of multiple fainter sources (Cañameras et al. 2015; *Planck* Collaboration XXVII 2015; Harrington et al. 2016), and only a detailed follow-up study can verify their nature. Three of our *Planck* candidates are associated with two distinct *WISE* counterparts that are high-redshift DSFGs (see Appendix B), and the number of 'confirmed' sources depends on whether one is counting the PCCS sources or the *WISE* sources.

By keeping the catalogue filtering as general as possible, our sample definition is relatively free of any systematic bias, but the large systematic uncertainty in the *Planck* photometry is a major limitation in defining the source completeness. As a result, any source statistics quoted here are strictly lower limits. The work presented here focuses mainly on identifying high-redshift DSFGs with apparent $L_{\rm IR} \geq 10^{13-14}$ $L_\odot$ and understanding their nature.

2.4 Comparison with independent Planck–Herschel samples

Our initial exploratory study of high-redshift *Planck* sources using the *Herschel* selection and the *LMT* follow-up observations have been reported by Harrington et al. (2016). Eight PCCS1 *Planck* sources associated with individual *Herschel* sources brighter than 100 mJy in archival *Herschel* SPIRE 857 GHz images were confirmed to be high-redshift DSFGs using the AzTEC and RSR instruments on the *LMT*. Their apparent IR luminosity of $(0.1-2.9)\times10^{14}$ $L_\odot$ and inferred $SFR = (1.5-30)\times10^3$ $M_\odot$ yr^{-1} are so extreme that strong magnification by gravitational lensing is naturally suspected and is later confirmed with the *HST* (Lowenthal et al., in preparation) and ALMA observations (this study).

All eight high-redshift *Planck* sources identified using the *Herschel* data are detected by *WISE* with SNR ≥5 in both *W*1 and *W*2 bands, and our *WISE* colour–magnitude filter discussed above would have recovered seven of the sources (see Fig. 4). The only exception is PJ132302.9, whose SED shown in fig. 5 by Harrington et al. (2016) indicates that its *WISE W*1 and *W*2 band photometry is dominated by the foreground $z \approx 0.5$ lensing galaxy. This outcome suggests that our *WISE* colour filtering may exclude a small fraction of candidates with a bright foreground lensing galaxy.

Among the 11 *Planck* sources analysed by Cañameras et al. (2015), six sources are drawn from the PCCS1 catalogue, and five of those overlap with the Harrington et al. sample. The lone exception, PJ105322.5, did not make the Harrington et al. sample because its dust peak shifted out of the *Planck* 857 GHz band due to its high-redshift ($z = 3.55$). This source is recovered by this study as one of the 545 GHz-selected (857 GHz drop-out) high-redshift *Planck* source that also satisfies our *WISE* colour–magnitude selection (see below). Two additional sources studied by Cañameras et al. are found in the PCCS2 catalogue, and they are also recovered by this study (see below) while the remaining three are missed by both PCCS1 and PCCS2 catalogues.

2.5 Other Planck-selected DSFGs in the literature

Aside from the *Planck–Herschel* sources studied by Cañameras et al. (2015) and Harrington et al. (2016), and one *Planck–Herschel* source found in the *Planck* Early Release Compact Source Catalogue studied by Herranz et al. (2013), cross-checking our final list of *Planck–WISE*-selected high-redshift source candidates using the NED has yielded several matches with known high-redshift galaxies. One well-studied example is *Planck–WISE* source PJ213511.6−010252 which is the $z = 2.326$ lensed SMG also known as 'Cosmic Eyelash' (Ivison et al. 2010; Swinbank et al. 2010). The *Planck–WISE* source PJ213512.7−010144 also falls within the same PCCS error ellipse, and this $z = 3.074$ lensed SMG found in a Lyman break galaxy search ('Cosmic Eye', Coppin et al. 2007; Smail et al. 2007) likely contributes to the *Planck* detection as well. The *Planck–WISE* source PJ090403.9+005619 is a candidate lensed high-redshift source found by the *Herschel*–ATLAS survey with a photometric redshift of $z_{\rm ph} = 1.7$ (González-Nuevo et al. 2012). Archival *Herschel*/SPIRE images show an extended, clumpy source in several *Herschel* bands, and it is likely an overdensity of sources, rather than a single bright source (see Table 3 and Section 5.1.2). The *Planck–WISE* source PJ132630.3+334407, which we report here with a detailed study, was first studied as a $z = 2.951$ lensed *Herschel*–ATLAS source by Bussmann et al. (2013, see Appendix B). Given the extremely small number density of $\sim10^{-2}$ per square degree for the *Planck*-selected DSFGs, finding only a handful of counterparts in the *entire* extragalactic fields studied by *Herschel* covering ≈1000 square degree in total area is about as expected. It also follows that the vast majority of the known high-redshift *Herschel* sources are too faint to be detected individually by *Planck* (see further discussions in Section 5).

Other large-area submillimetre cosmology experiments such as the *SPT* survey and the *ACT* survey should include a few *Planck–WISE* sources as well. The $z = 2.515$ *Planck–WISE* source PJ012507.1−472356 (SPT0125−47), the $z = 2.783$ source

Downloaded from https://academic.oup.com/mnras/article/515/3/3911/6603847 by guest on 28 January 2026

PJ053816.8−503052 (SPT0538−50), and the $z = 2.726$ source PJ233226.5−535839 (SPT2332−53) are three of the 81 dust-dominated sources identified in the 2500 square degree survey fields (Vieira et al. 2010; Greve et al. 2012; Weiß et al. 2013; Reuter et al. 2020). The list of 30 brightest DSFGs found in the *ACT* survey (480 square degree in area, Gralla et al. 2020) includes three *Planck–WISE* sources that are already known: Cosmic Eyelash (PJ213511.6−010252, discussed earlier), PJ020941.3+001559 (Geach et al. 2015; Harrington et al. 2016), and PJ231356.6+010918 (this study).

The *Planck* and *Herschel* photometry of the four additional high-redshift *Planck*-selected DSFGs identified in the literature are included in Table 3, and they are also shown in Fig. 3 along with the *Herschel*-selected sources to show the parameter space they occupy in these colour–magnitude plots. They are included in the entire *Planck–WISE* sample used to characterize the properties of the *Planck*-selected DSFG population as a whole later in Section 5. While this paper is undergoing a referee review, Trombetti et al. (2021) posted on the arXiv.org preprint server a paper reporting a search for candidate strongly lensed dusty galaxies in the *Planck* catalogues using a similar SED analysis method utilizing more recent *Planck* photometry products, trained using a sample of known *Planck*-selected DSFGs including most of the sources reported here. Their follow-up confirmation work has started, and a future comparison of the two methods should prove interesting.

3 LMT AND ALMA OBSERVATIONS

An observational program to confirm the 118 *Planck*-selected DSFGs candidates identified with the *WISE* colour–magnitude filter (described in Section 2.2) is carried out through AzTEC 1.1 mm continuum camera imaging and CO spectroscopy using the RSR on the *LMT*. This is a long-term observational program, and here we report the initial confirmations of 24 DSFGs.

The design of the *LMT* confirmation programme was to start with AzTEC snapshot observations and follow-up spectroscopy using the RSR, but the limited availability of the AzTEC instrument due to weather conditions and instrument readiness forced us to proceed with RSR spectroscopy without any AzTEC prior. A total of 24 CO line sources are confirmed so far, including 22 $z \gtrsim 1$ DSFGs and two ULIRGs at $z \sim 0.2$. Essentially an independent AzTEC photometry campaign conducted in parallel detected 11 high-redshift DSFGs confirmed with RSR CO detection.

Here, we also present the 1.1 mm continuum imaging results from our Cycle 5 ALMA programme that was designed to map the distribution of dust continuum and CO line emission in a selected subset of 12 *Planck*-selected DSFGs reported here. These ALMA observations provide independent 1.1 mm photometry of 12 DSFGs, including six new 1.1 mm continuum measurements, and they are included in the broad-band SED analysis.

3.1 AzTEC 1.1 mm continuum observations

AzTEC 1.1 mm continuum observations were made with the AzTEC camera (Wilson et al. 2008), which is a facility instrument on the *LMT* (Hughes et al. 2020). During the observing period between 2014 March and 2016 May, only the inner 32 m diameter area of the primary mirror was illuminated, leading to an effective beam of 8.5 arcsec (FWHM). A modified Lissajous pattern is used to image a uniform sensitivity area of 1.5 arcmin diameter centred on the *WISE* source position. Each source was observed with an on-source integration time of 10 min each. Each target observation was bracketed by observations of a nearby bright quasar ($\leq 20^\circ$ away) to ensure the pointing accuracy of better than 1.5 arcsec. The data for each source were reduced using the AzTEC Standard Pipeline described by Wilson et al. (2008) and Scott et al. (2008), using the Wiener filtering optimized for point source detection (Perera et al. 2008). The resulting noise in the AzTEC images is in the range of $\sigma = 1.0$–3.1 mJy depending on the total integration time and weather conditions.

A total of 30 sources identified by the *Planck–WISE* selection were observed, and 13 sources (43 per cent) are clearly detected. The details of the AzTEC observations and the derived 1.1 mm photometry are summarized in Tables 2 and 3 while the details of the 17 sources without a bright compact counterpart are given in Appendix A (see Table A1). The 1.1 mm flux density measured for the 13 detected sources ranges between 15 and 202 mJy, comparable to those of the eight *Planck* sources we previously identified using *Herschel* data (Harrington et al. 2016, $S_{1.1\mathrm{mm}} = 8$–147 mJy). The 17 sources undetected by AzTEC have 3σ upper limits between 3.2 and 9.3 mJy, and these measurements rule out the detected *Planck* emission originating from a single bright IR source.

The AzTEC 1.1 mm continuum images are shown in contours over the grey-scale *WISE* 22 μm (*W*4) band images in Fig. 5. All but two of the sources have a compact morphology, consistent with being unresolved by the 8.5 arcsec AzTEC beam. The two extended AzTEC sources, PJ074852.6 and PJ154432.4, are associated with a crowded foreground galaxy concentration, and their dust continuum emission is extended over 10 arcsec scales (see Appendix B for further discussions).

This 43 per cent AzTEC confirmation rate indicates that our candidate list includes a significant number of foreground confusing sources even after the extensive vetting described in Section 2. Since our candidate selection requires an inclusion in at least two PCCS bands, each with $\geq 7\sigma$ statistical significance, they are not likely spurious sources. Instead, *Planck* sources that are not a single bright AzTEC source are likely extended or distributed dust sources – extended emission is obvious in some cases. Some *Planck* candidates are likely foreground cirrus clouds with an arcmin-scale structure that survived our filtering. Previous studies of *Planck*-selected sources have also shown some to be overdensity of fainter high-redshift DSFGs (Clements et al. 2014, 2016; Flores-Cacho et al. 2016), rather than a single bright object.

3.2 RSR CO spectroscopy

The RSR (Erickson et al. 2007) is an *LMT* facility broad-band spectrometer system that operates in the frequency window of 73–111 GHz, with four detector pixels organized in a dual–beam, dual–polarization configuration. The RSR beam-switches at 1 kHz frequency between the two beams separated by 78 arcsec in Azimuth direction, and this rapid differencing leads to a stable and flat baseline across its ultrawide bandwidth. Its back-end spectrometer covers the entire 38 GHz bandwidth with a spectral resolution of 31.25 MHz (102 km s^{-1} at 92 GHz). We expect to detect at least one of the low-*J* ($J_{\mathrm{up}} = 2$–4) CO transitions to yield the redshifts of our targets. Table 2 provides information on the integration time for each source. For the majority of the sources a CO line was evident within 15 min of integration, and a longer integration (30–75 min) was used to yield a secure CO line detection with a *S*/*N* ratio ≥ 7 in all cases.

The measured RSR spectra of all 24 observed sources are shown in Fig. 6, and the measured and derived CO line quantities are summarized in Table 4. The design of the experiment was to target the sources confirmed to be a bright AzTEC 1.1 mm source, but high priority candidates without any AzTEC observations were also targeted

Downloaded from https://academic.oup.com/mnras/article/515/3/3911/6603847 by guest on 28 January 2026

Table 2. Summary of *LMT* observations.

Source ID	RA (J2000)	DEC (J2000)	RSR Dates	RSR Int. time (min)	AzTEC Dates	AzTEC Int. time (min)
PJ011646.8	01h16m46.8	−24d37m02s	2015-12-18	30	–	–
PJ014341.2	01h43m41.2	−01d47m26s	2015-12-08, 2015-12-18	75	–	–
PJ022634.0	02h26m34.0	+23d45m28s	2016-02-03	15	2016-01-24	10
PJ030510.6	03h05m10.6	−30d36m30s	2016-02-02, 2016-02-03	30	2016-02-05	10
PJ074851.7	07h48m51.7	+59d41m54s	2016-02-01	30	–	–
PJ074852.6	07h48m52.6	+59d42m09s	2016-01-30, 2016-02-01	60	2016-01-24	10
PJ084648.6	08h46m48.6	+15d05m57s	2016-01-16, 2016-02-02	60	2016-01-22	10
PJ084650.1	08h46m50.1	+15d05m47s	2015-12-15	45	2014-11-10	10
PJ105322.6	10h53m22.6	+60d51m47s	2015-12-16, 2016-02-01	60	2016-01-23	10
PJ112713.4	11h27m13.4	+46d09m24s	2015-12-15	30	–	–
PJ113805.5	11h38m05.5	+32d57m57s	2015-06-16, 2015-06-18	30	–	–
PJ113921.7	11h39m21.7	+20d24m51s	2016-02-03	30	2016-02-05	10
PJ114038.5	11h40m38.5	+53d21m57s	2015-12-18	30	–	–
PJ114329.5	11h43m29.5	+68d01m07s	2015-12-18, 2016-01-27, 2016-02-07	60	–	–
PJ132217.5	13h22m17.5	+09d23m26s	2016-02-20, 2015-06-10	60	–	–
PJ132630.3	13h26m30.3	+33d44m07s	2014-05-05, 2014-05-23	60	–	–
PJ132934.2	13h29m34.2	+22d43m27s	2016-02-17, 2016-02-19	50	2016-01-22	10
PJ132935.3	13h29m35.3	+22d43m24s	2016-02-18	30	–	–
PJ133634.9	13h36m34.9	+49d13m14s	2016-02-07	30	2016-01-22	10
PJ141230.5	14h12m30.5	+50d34m55s	2015-05-12	45	–	–
PJ144653.2	14h46m53.2	+17d52m33s	2016-02-19	30	2016-01-22	10
PJ144958.6	14h49m58.6	+22d38m37s	2015-05-12	45	2016-01-23	10
PJ154432.4	15h44m32.4	+50d23m44s	2015-01-29	30	2016-01-23	10
PJ231356.6	23h13m56.6	+01d09m18s	2015-05-20, 2015-06-13, 2015-06-16	75	–	–

Table 3. Summary of *Planck*, *Herschel*, AzTEC, and ALMA photometry.

Source ID	$Planck_{350}$ (mJy)	$Planck_{500}$ (mJy)	$Planck_{850}$ (mJy)	$SPIRE_{250}$ (mJy)	$SPIRE_{350}$ (mJy)	$SPIRE_{500}$ (mJy)	S_{850} (mJy)	$AzTEC_{1100}$ (mJy)	$ALMA_{1100}$ (mJy)	References
PJ011646.8	513 ± 462	555 ± 336	–	–	–	–	–	–	66 ± 10	–
PJ014341.2	441 ± 336	–	–	210 ± 21	149 ± 25	82 ± 22	–	–	4.0 ± 0.6	–
PJ022634.0	1804 ± 1241	1113 ± 381	433 ± 185	–	–	–	–	103 ± 15	–	–
PJ030510.6	706 ± 194	375 ± 177	–	–	–	–	–	50 ± 10	48 ± 7	–
PJ074851.7	997 ± 593	737 ± 229	351 ± 123	–	–	–	–	66 ± 10	–	–
PJ084650.1	1748 ± 322	1167 ± 240	500 ± 91	–	–	–	–	118 ± 15	76 ± 11	–
PJ105322.6	–	680 ± 127	356 ± 52	460 ± 46	739 ± 74	771 ± 77	360 ± 36	202 ± 30	–	1
PJ112713.4	195 ± 127	<330	–	–	–	–	–	–	–	–
PJ113805.5	232 ± 145	93 ± 90	57 ± 50	–	–	–	–	–	9.5 ± 1.4	–
PJ113921.7	406 ± 312	343 ± 312	–	300 ± 30	397 ± 40	341 ± 34	111 ± 12	58 ± 12	49 ± 7	1
PJ114038.5	413 ± 258	185 ± 152	–	–	–	–	–	–	–	–
PJ114329.5	439 ± 326	349 ± 226	111 ± 75	–	–	–	–	–	–	–
PJ132217.5	717 ± 191	322 ± 152	–	–	–	–	–	–	13 ± 2	–
PJ132630.3	282 ± 200	–	148 ± 89	197 ± 20	288 ± 29	288 ± 29	65 ± 7	–	28 ± 4	3
PJ132934.1	1298 ± 219	713 ± 139	263 ± 88	–	–	–	128 ± 20	60 ± 10	51 ± 8	2
PJ133634.9	627 ± 140	313 ± 154	166 ± 82	–	–	–	–	65 ± 12	–	–
PJ141230.5	944 ± 195	338 ± 156	354 ± 75	–	–	–	–	–	–	–
PJ144653.2	1149 ± 588	615 ± 284	113 ± 86	–	–	–	–	15 ± 3	17 ± 3	–
PJ144958.6	668 ± 166	457 ± 160	230 ± 107	–	–	–	–	37 ± 8	37 ± 6	–
PJ154432.4	–	485 ± 265	303 ± 93	225 ± 23	353 ± 35	353 ± 35	87 ± 11	35 ± 10	–	1
PJ231356.6	393 ± 266	234 ± 224	–	–	–	–	–	–	26 ± 4	6
Planck sources from literature										
Cosmic Eyelash	1393 ± 416	919 ± 201	475 ± 81	372 ± 22	453 ± 26	365 ± 18	106 ± 7	–	–	4,5,6
PJ090403.9	1493 ± 393	708 ± 232	–	104 ± 7	87 ± 8	50 ± 9	–	–	–	7
SPT0125−47	903 ± 113	600 ± 256	367 ± 69	848 ± 11	817 ± 17	546 ± 17	–	–	–	8
SPT0538−47	844 ± 215	426 ± 126	–	391 ± 10	484 ± 14	377 ± 13	–	–	–	9

Notes. Names of the photometry bands are listed in micron rather than GHz in order to be consistent with the data table in our earlier paper by Harrington et al. (2016). The listed uncertainty on the AzTEC and ALMA photometry includes 15 per cent systematic uncertainty in the absolute flux calibration. The large uncertainties in the *Planck* photometry reflect the systematic uncertainty associated with the source confusion (see Section 4.1 for details). References: (1) Cañameras et al. (2015); (2) Díaz-Sánchez et al. (2017); (3) Bussmann et al. (2013); (4) Ivison et al. (2010); (5) Swinbank et al. (2010); (6) Gralla et al. (2020); (7) González-Nuevo et al. (2012); (8) Weiß et al. (2013); (9) Greve et al. (2012).

Downloaded from https://academic.oup.com/mnras/article/515/3/3911/6603847 by guest on 28 January 2026

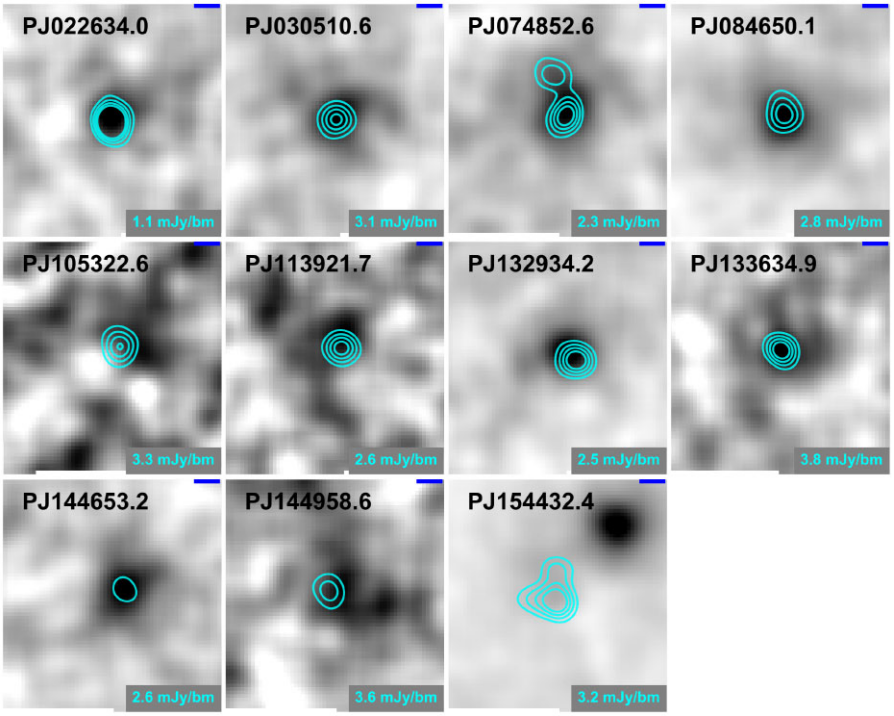

Figure 5. AzTEC 1.1 mm images at 8.5 arcsec resolution shown in contours over the *WISE* 22 μm images in grey-scale. Each square box is 90 arcsec on each side. Contour levels correspond to 5σ, 10σ, 15σ, and 20σ (σ values are given on the bottom-right corner of each frame). The orientation of the images is such that north is up while east is to the left. PJ084648.6 is in the same frame as PJ084650.1, but the peak is less than 5σ and is not shown.

to facilitate the survey scheduling. As a result, all 13 sources detected by AzTEC have a CO redshift and luminosity, while 11 additional sources were observed based on our *WISE* colour selection alone.

As discussed in detail by Yun et al. (2015), two or more CO transitions fall within the RSR spectral band at $z \geq 3.15$, and an unambiguous redshift for a CO source can be determined from the RSR spectrum alone. For PJ105322.6, PJ133634.9, and PJ141230.5, both CO (3–2) and CO (4–3) lines are detected, and their redshifts are unambiguously determined. For PJ011646.7 and PJ144958.6, CO (2–1) and CO (3–2) lines are detected in their RSR spectra, also yielding an unambiguous redshift, although their CO (2–1) is too close to the spectrum edge to yield usable line information. For the remaining 19 targets, only a single CO line is detected, and their redshifts are assigned based on the photometric redshift support, as discussed by Harrington et al. (2016). The single CO lines detected for PJ114038.5 and PJ114329.5 correspond to the CO (1–0) transition at the optical spectroscopic redshifts of the *WISE* sources reported by the SDSS, and we conclude that they are foreground ULIRGs at $z \approx 0.2$, rather than high-redshift sources. For the remaining sources, their single line redshifts are confirmed for all but two cases by detecting other CO transitions using the *IRAM* 30 m telescope and the *GBT*, and those results are presented elsewhere (Harrington et al. 2021, also see Table 4 and Appendix B). The single line redshifts of PJ014341.2 and PJ144653.2 remain to be confirmed.

Despite the coarse spectral resolution of the RSR, all of the CO lines are clearly resolved. The CO line-widths ΔV reported in Table 4 are derived by fitting a Gaussian to the measured spectra and applying a correction for the instrumental resolution (see Harrington et al. 2016 for details). The uncertainty in the reported line-widths reflects both the SNR of the spectra and the formal uncertainty in the spectral resolution correction. The measured CO line-widths range between 150 and 637 $\mathrm{km\,s^{-1}}$, comparable to the values reported for similar objects (e.g. Cañameras et al. 2015; Harrington et al. 2016).

The CO line luminosity, L'_{CO}, is computed using equation (3) by Solomon et al. (1997).[8] Molecular gas mass M_{H2} is derived first by converting the line luminosity to $L'_{\mathrm{CO(1-0)}}$ using the average 'SMG' ratios of $L'_{\mathrm{CO(2-1)}}/L'_{\mathrm{CO(1-0)}} = 0.85$, $L'_{\mathrm{CO(3-2)}}/L'_{\mathrm{CO(1-0)}} = 0.66$, and $L'_{\mathrm{CO(4-3)}}/L'_{\mathrm{CO(1-0)}} = 0.46$ (Carilli & Walter 2013) and then applying the standard CO-to-H_2 conversion factor of $\alpha_{\mathrm{CO}} = 4.3$ $\mathrm{M_\odot}$ $[\mathrm{K\,km\,s^{-1}\,pc^2}]^{-1}$ (Bolatto, Wolfire & Leroy 2013). A recent analysis of the literature data by Kirkpatrick et al. (2019) suggests the mean CO excitation relations can vary by up to 10 per cent, depending on the sample definition. While some authors have advocated a 'ULIRG' (e.g. $\alpha_{\mathrm{CO}} \approx 1$) or other CO-to-$H_2$ conversion relations for various reasons, there are no compelling reasons to believe they are any more accurate (see the detailed discussions by Scoville et al. 2016). By obtaining new measurements of additional CO rotational transitions and analysing the gas excitation directly, Harrington et al. (2021) have obtained new gas mass estimates for 16 *Planck* sources in our sample, largely independent of these standard assumptions, and they are discussed further in Section 5.2.

The derived molecular gas masses are in the range of $M_{\mathrm{H2}} = (0.5 - 93) \times 10^{11} \mu^{-1}$ $\mathrm{M_\odot}$ (uncorrected for an unknown magnification factor μ) with a median value of $M_{\mathrm{H2}} = 28 \times 10^{11} \mu^{-1}$ $\mathrm{M_\odot}$. If they are all strongly magnified with $\mu \sim 10$ (see the discussion in Section 5.1.2), then their intrinsic gas masses are comparable to those of other SMGs reported previously using similar assumptions (see review by Carilli & Walter 2013).

[8]The RSR spectra measured in T_{A}^* unit are converted to flux density unit (Jy) using a frequency-dependent conversion relation, $\mathrm{Jy/K} = 0.027 * \nu_{\mathrm{GHz}} + 3.36$ for the 32 m diameter area illuminated (Yun et al. 2020).

Downloaded from https://academic.oup.com/mnras/article/515/3/3911/6603847 by guest on 28 January 2026

Table 4. Summary of RSR measurements.

Source ID	ν_{CO} (GHz)	Line	z_{CO}	ΔV (km s^{-1})	$S\Delta V$ (Jy km s^{-1})	$\mu L'_{CO}$ (10^{10} K km s^{-1} pc^2)	μM_{H2} (10^{10} M$_\odot$)	μM_{gas}[a] (10^{10} M$_\odot$)	Notes
PJ011646.8	110.660	CO (3–2)	2.1249 ± 0.0002	352 ± 5	33.2 ± 2.6	81 ± 4	524 ± 50	473 ± 547	(1)
PJ014341.2	110.002	CO (2–1)	1.0956 ± 0.0003	622 ± 22	10.6 ± 0.7	17 ± 2	85 ± 15	–	(2)
PJ022634.0	83.924	CO (3–2)	3.1203 ± 0.0002	502 ± 7	29.1 ± 0.8	136 ± 8	886 ± 133	227 ± 280	(1)
PJ030510.6	105.981	CO (3–2)	2.2628 ± 0.0003	283 ± 7	9.7 ± 1.2	26 ± 3	169 ± 21	145 ± 35	(1)
PJ074851.7	92.079	CO (3–2)	2.7554 ± 0.0003	578 ± 8	15.0 ± 0.8	57 ± 5	371 ± 40	294 ± 400	(1)
PJ074852.6	92.079	CO (3–2)	2.7554 ± 0.0003	607 ± 12	12.1 ± 1.1	46 ± 4	300 ± 53	–	(1)
PJ084648.6	94.374	CO (3–2)	2.6641 ± 0.0004	593 ± 14	12.5 ± 0.6	45 ± 4	293 ± 49	–	(1)
PJ084650.1	94.464	CO (3–2)	2.6606 ± 0.0002	502 ± 10	12.8 ± 0.4	46 ± 3	300 ± 53	212 ± 171	(1)
PJ105322.6	76.016	CO (3–2)	3.5490 ± 0.0003	568 ± 7	24.4 ± 0.7	142 ± 9	928 ± 139	1550 ± 360	(3)
	101.363	CO (4–3)	3.5488 ± 0.0003	495 ± 7	25.8 ± 0.6	85 ± 5	795 ± 119	–	–
PJ112713.4	100.100	CO (2–1)	1.3029 ± 0.0002	496 ± 12	8.7 ± 0.6	19 ± 3	70 ± 13	110 ± 12	(1)
PJ113805.5	76.364	CO (2–1)	2.0190 ± 0.0002	154 ± 9	4.9 ± 0.6	15 ± 2	77 ± 11	36 ± 38	(1)
PJ113921.7	89.624	CO (3–2)	2.8583 ± 0.0005	496 ± 14	11.5 ± 1.2	40 ± 6	265 ± 39	311 ± 54	(1), (3)
PJ114038.5	98.933	CO (1–0)	0.1652 ± 0.0001	589 ± 14	13.0 ± 0.6	1.6 ± 0.1	7.1 ± 1.6	–	(4)
PJ114329.5	95.125	CO (1–0)	0.2118 ± 0.0001	279 ± 8	4.7 ± 0.5	1.3 ± 0.1	5.3 ± 0.8	–	(4)
PJ132217.5	75.151	CO (2–1)	2.0676 ± 0.0001	158 ± 4	7.2 ± 0.6	38 ± 3	192 ± 30	50 ± 96	(1)
PJ132630.3	87.519	CO (3–2)	2.9511 ± 0.0002	292 ± 5	9.8 ± 0.5	43 ± 3	280 ± 45	140 ± 20	(1)
PJ132934.2	75.839	CO (2–1)	2.0398 ± 0.0001	476 ± 4	36.1 ± 1.6	180 ± 8	910 ± 137	162 ± 48	(1), (5)
PJ132935.3	75.829	CO (2–1)	2.0402 ± 0.0002	474 ± 9	15.5 ± 0.9	77 ± 5	390 ± 59	–	(1)
PJ133634.9	81.280	CO (3–2)	3.2541 ± 0.0004	638 ± 12	16.9 ± 1.1	86 ± 8	563 ± 85	179 ± 54	(1)
	108.370	CO (4–3)	3.2543 ± 0.0003	532 ± 6	21.9 ± 1.1	60 ± 5	557 ± 84	–	–
PJ141230.5	80.224	CO (3–2)	3.3103 ± 0.0004	451 ± 14	7.1 ± 0.6	38 ± 5	247 ± 36	–	–
	106.948	CO (4–3)	3.3105 ± 0.0005	540 ± 22	11.6 ± 0.9	33 ± 3	311 ± 47	–	–
PJ144653.2	110.598	CO (2–1)	1.0844 ± 0.0001	458 ± 8	16.5 ± 0.6	42 ± 3	137 ± 20	–	(2)
PJ144958.6	109.666	CO (3–2)	2.1533 ± 0.0002	387 ± 8	10.8 ± 0.7	26 ± 2	167 ± 29	152 ± 114	(1)
PJ154432.4	96.092	CO (3–2)	2.5989 ± 0.0003	407 ± 12	9.7 ± 0.5	32 ± 3	208 ± 32	326 ± 33	(3)
PJ231356.6	107.550	CO (3–2)	2.2167 ± 0.0002	247 ± 14	10.7 ± 0.7	28 ± 2	184 ± 28	299 ± 524	(1)

Notes. (1) *IRAM* 30 m and *Green Bank Telescope (GBT)* confirmations by Harrington et al. (2021); (2) for the single line detections of PJ014341.2 and PJ144653.2, alternative redshifts are $z = 2.144$ and $z = 2.127$ if the detected line is the CO (3–2) transition; (3) Cañameras et al. (2015); (4) optical redshifts from the Sloan Digital Sky Survey (SDSS); (5) Díaz-Sánchez et al. (2017). *Note.*
[a]M_{gas} is total cold gas mass derived using a full radiative transfer modelling of the multiple CO, [C I], and dust continuum measurements by Harrington et al. (2021).

3.3 ALMA 1.1 mm continuum observations

ALMA 260 GHz (band 6) observations of the 12 *Planck*-selected DSFGs have been obtained as part of the 2017.1.01214.S programme (PI: M. Yun) between 2018 March 27 and August 31. The default continuum dual polarization set-up with a total bandwidth of 8 GHz (250–254 GHz and 266–270 GHz) is used, with a target synthesis beam of $\theta \approx 0.4$ arcsec.

The ALMA 260 GHz continuum images are shown in contours over the *HST*/WFC3 F160W grey-scale images (Lowenthal et al., in preparation) in Fig. 7. All of the sources are clearly resolved by ALMA, in many cases showing the classic morphology of Einstein rings and lensed arcs. Sources such as PJ011646.7 and PJ014342.2 are lensed primarily by a single massive galaxy, while others such as PJ132217.5 are likely lensed by a small galaxy group. Some of the large lensed arcs such as PJ084648.5, PJ132934.2, and PJ144958.5 are likely lensed by a massive galaxy group or a galaxy cluster. Two objects, PJ030510.6 and P113805.5, are compact with a source size of only ∼1 arcsec, but the CO line images obtained in the same ALMA programme (not shown here) display the characteristic Einstein ring morphology. Dust continuum features often have an associated stellar feature in the *HST* images, but they are frequently displaced from each other. There are also lensed stellar features without a dust continuum counterpart (e.g. P011646.7 and PJ132217.5), indicating that either the stellar light is more extended than the gas and dust, or the lensed galaxy has multiple components or stellar companions. The stellar light along the ALMA dust continuum peaks is strongly suppressed or is entirely missing in many cases (e.g. PJ084648.6 and PJ113921.7).

The measured ALMA 260 GHz (1100 μm) flux densities are listed in the last column of Table 3, adjacent to the AzTEC 1100 μm flux density. Six sources are observed by both ALMA and AzTEC (see Fig. 8), and the total 260 GHz flux density measured by ALMA agrees well with AzTEC measurements in most cases. This indicates that our ALMA observations are sensitive to and are capable of recovering the entire 1 mm continuum flux detected by AzTEC, despite its nearly 30 times higher angular resolution. One possible exception is the brightest source PJ084650, which is a large lensed arc system with multiple components including a 6 arcsec long arc (see top-right panel of Fig. 7). Its total measured ALMA 260 GHz flux of 76 ± 11 mJy is 36 per cent smaller than the total flux measured by AzTEC, and this 'missing flux' is an expected result since the largest angular scale recoverable by the ALMA configuration used is ∼4 arcsec.

4 SED ANALYSIS OF THE PLANCK SOURCES

4.1 Summary of multiwavelength photometry

The *Planck*, *Herschel*, AzTEC, and ALMA photometry of the *Planck*–*WISE* DSFGs is summarized in Table 3. Their SEDs mapped by these bands contain the bulk of their bolometric luminosity, as shown in Fig. 9. The AzTEC and ALMA 1.1 mm photometry

Downloaded from https://academic.oup.com/mnras/article/515/3/3911/6603847 by guest on 28 January 2026

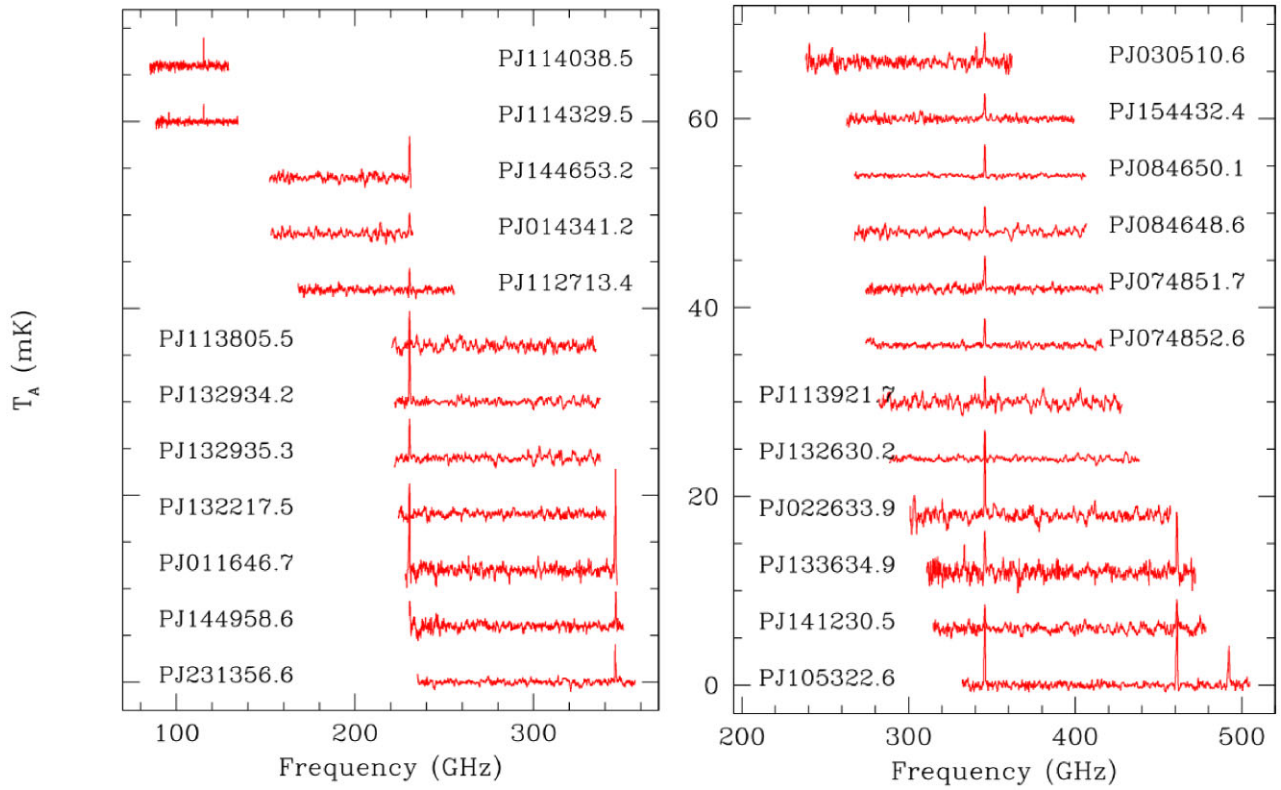

Figure 6. The RSR spectra of 24 *Planck*-selected sources in their rest frame. They are sorted by their redshift, and two CO lines are detected for three of the highest redshift sources, yielding a secure redshift. The highest redshift source also shows the redshifted 492 GHz [C I] line as well.

('$AzTEC_{1100}$' and '$ALMA_{1100}$') is already discussed in some detail above. Here, we discuss briefly the *Planck*, *Herschel*, *WISE*, and 20 cm radio continuum photometry obtained from archives and literature (see Table 5). In most cases, the uncertainty on photometry reported is dominated by systematic uncertainties, such as the source confusion for the *Planck* photometry and absolute flux calibration uncertainty for all other photometry.

***Planck* photometry**: The *Planck* 857 GHz (350 μm, '$Planck_{350}$'), 545 GHz (500 μm, '$Planck_{500}$'), and 353 GHz (850 μm, '$Planck_{850}$') flux densities reported in Table 3 are the *Planck* aperture photometry (APERFLUX) values in the PCCS2.[9] The PCCS2 includes four different estimates of source flux: detection pipeline photometry (DETFLUX), aperture photometry (APERFLUX), point spread function fit photometry (PSFFLUX), and Gaussian fit photometry (GAUFLUX). DETFLUX is suggested as the flux estimation method of choice for unresolved sources in regions of low background, given its greater sensitivity. The internal consistency check has shown that DETFLUX is subject to a greater scatter and a significant flux bias. In addition, an external consistency check by comparing *Planck* and *Herschel* data indicates a greater reliability for APERFLUX over DETFLUX (Planck Collaboration XXVI 2016). Therefore, we adopt the APERFLUX for *Planck* band photometry in our analysis. For the five *Planck*–*WISE* sources with published *Herschel* photometry, *Planck* photometry is consistent with the higher resolution *Herschel* data (see Table 3). The agreement between the *Planck* 353 GHz photometry and the published SCUBA-2 photometry (Cañameras et al. 2015; Díaz-Sánchez et al. 2017) is not as good for the five sources in common, and there might be some systematic problems with either set of photometry data. As discussed in Section 2.5, two *Planck* sources found in the literature (Cosmic Eyelash and PJ090403.9) included in Table 3 are in crowded fields with multiple *Herschel* sources, and the discrepancy between *Planck* and *Herschel* can be explained by this source blending.

***Herschel* photometry:** The *Herschel Space Observatory* and its dedicated 'large-area' surveys such as the *Herschel* ATLAS (H-ATLAS, Eales et al. 2010) and the *Herschel* Multi-tiered Extragalactic Survey (Oliver et al. 2012) covered less than 10 per cent of the extragalactic sky in total. Therefore, only a small fraction of *Planck*-selected high-redshift candidates are expected to have *Herschel* photometry. We found *Herschel* photometry of a total of five *Planck*-selected sources in the NASA/IPAC Infrared Science Archive (IRSA), and they are included in Table 3. PJ014341.2 and PJ132630.3 are located in the survey areas covered by the *Herschel* Stripe 82 Survey (Viero et al. 2014) and the H-ATLAS (Eales et al. 2010), respectively, while the three remaining sources (PJ105322.6, PJ113921.7, and P154432.4) are among the 200 *Planck* sources targeted as part of the 'must-do' Director's Discretionary Time (DDT) programme (Cañameras et al. 2015). Excluding the three sources specifically targeted by the *Herschel* DDT programme, only two out of 19 PCCS high-redshift sources we identified have a chance coverage by the existing *Herschel* archive, and this supports our main motivation for using the *Planck* survey data itself for finding the brightest high-redshift IR sources.

***WISE* photometry**. Near-IR colour is one of the key discriminators for heavily obscured starburst galaxies in our high-redshift candidate selection (see Section 2.2). The *WISE* photometry used in this process comes from the *WISE* all-sky survey (Wright et al. 2010). The relative sensitivity of the longer wavelength channels degrade rapidly with increasing wavelength – the 5σ detection limits of the

[9]The nomenclature for the *Planck* photometry in Table 3 uses the wavelength (i.e. 350, 500, and 850 μm), rather than the frequency designation, to be consistent with the convention used by Harrington et al. (2016).

Downloaded from https://academic.oup.com/mnras/article/515/3/3911/6603847 by guest on 28 January 2026

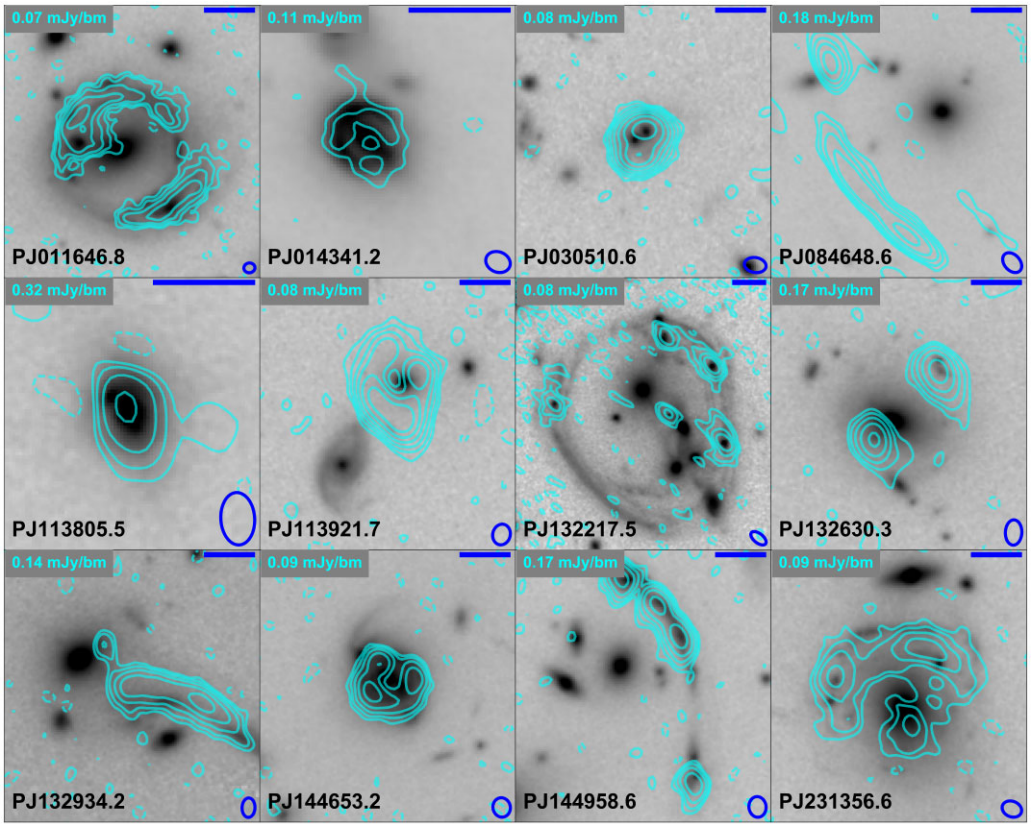

Figure 7. ALMA 260 GHz continuum images are shown in contours over the *HST*/WFC3 F160W grey-scale images (Lowenthal et al., in preparation) for the 12 *Planck* sources targeted by both surveys. Each frame is 10 arcsec in size in most cases, and a blue bar on the top-right corner is 2 arcsec in size. The ALMA beams are shown as an ellipse on the bottom-right corner. The contours shown are −2, 2, 4, 8, 16, 32, 64, and 128 times 1σ, which are indicated on the top-left corner in each frame.

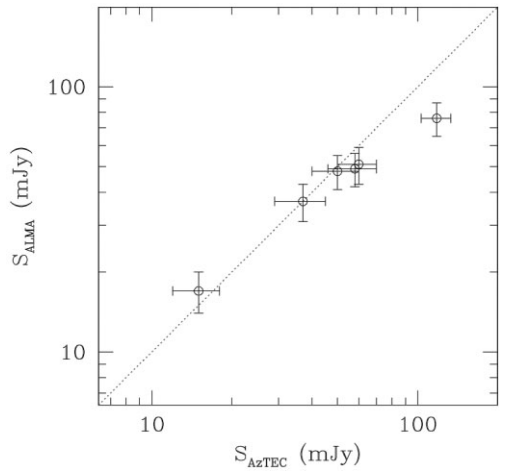

Figure 8. A comparison of the total ALMA 260 GHz flux density measured at $\theta \sim 0.4$ arcsec with those measured by AzTEC with the 8.5 arcsec beam at the *LMT*. The dotted diagonal line is a one-to-one correspondence line shown only to guide the eye.

catalogue are 0.068, 0.098, 0.86, and 5.4 mJy in the 3.4, 4.6, 11, and 22 μm bands, according to the Explanatory Supplement to the *WISE* All-Sky Data Release Products.[10] At the same time, the mid-IR SEDs of these *Planck*-selected high-redshift dusty starbursts are so steep and so bright that nearly all of them are also substantially detected in the 11 and the 22 μm bands as well – see Table 5 and also table 5 by Harrington et al. (2016).

20 cm radio continuum. The radio-FIR correlation is a well-established global relation for SFGs, rooted in the formation and evolution of massive stars (e.g. Condon 1992; Yun & Carilli 2002). If these *Planck*-selected high-redshift galaxies with extreme luminosity are powered by SF, they are also expected to follow the same radio-FIR correlation and should also be bright and detectable in radio continuum even by relatively shallow surveys. The 20 cm radio continuum photometry listed in Table 5 comes from either the NVSS (Condon et al. 1998) or the VLA FIRST (Becker, White & Helfand 1995). The majority of the high-redshift *Planck* sources are detected by the shallower, all-sky NVSS survey. Those located in the FIRST survey coverage are detected more securely with a higher resolution and SNR. Most detections and upper limits are consistent with their following the local radio-FIR correlation, as shown in Fig. 9, and suggest that the nature of the luminosity for these galaxies is consistent with being powered by a pure starburst in nearly all cases.

4.2 Modified blackbody model

We explore constraints on the IR luminosity and characterize the dust emission for these systems by analysing their SEDs using a modified blackbody model, which is a widely used characterization of dust

[10] http://wise2.ipac.caltech.edu/docs/release/allsky/expsup/index.html

Downloaded from https://academic.oup.com/mnras/article/515/3/3911/6603847 by guest on 28 January 2026

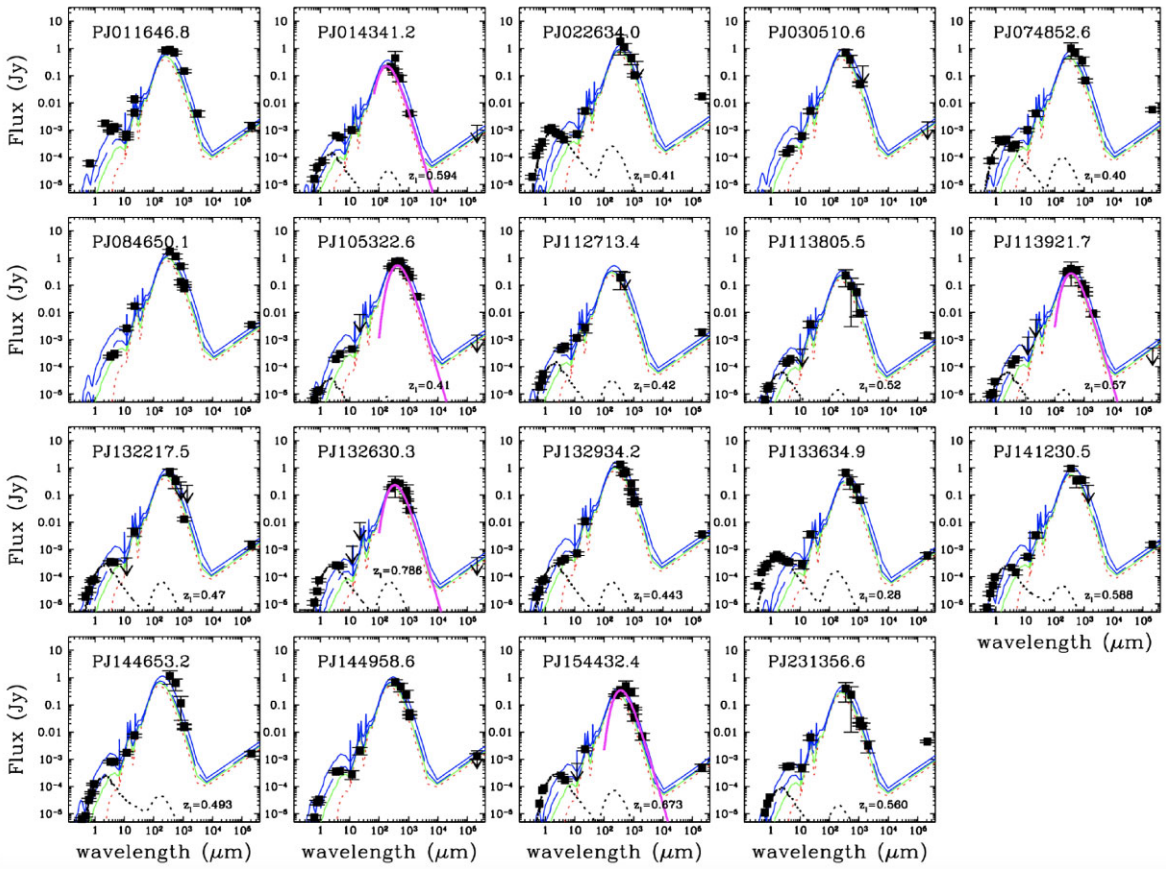

Figure 9. SEDs of the 19 new $z \geq 1$ *Planck* sources with photometry listed in Table 3. Two sources, PJ112713.4 and PJ114038.5, have only the RSR spectral line data aside from the *Planck* photometry, and their SEDs are now shown. The models shown are the best-fitting dusty starburst SEDs by Efstathiou, Rowan-Robinson & Siebenmorgen (2000) with an extension to the radio wavelengths (Yun & Carilli 2002) at their CO redshifts (see Table 4). Modified blackbody models fitting only the *Herschel* and AzTEC photometry are shown in thick magenta lines. An elliptical galaxy SED template by Polletta et al. (2007) covering the optical wavelength bands is also shown using a dashed line for the sources with an obvious foreground galaxy in the SDSS plates.

Table 5. Summary of *WISE* near-IR and Very Large Array (VLA) 20 cm photometry.

Source ID	$W_{3.4\mu}$ (mJy)	$W_{4.6\mu}$ (mJy)	$W_{11\mu}$ (mJy)	$W_{22\mu}$ (mJy)	$S_{20\mathrm{cm}}$ (mJy)
PJ011646.8	0.93 ± 0.09	1.17 ± 0.16	0.67 ± 0.13	13.4 ± 2.2	1.4 ± 0.5
PJ014341.2	0.63 ± 0.02	0.53 ± 0.02	0.98 ± 0.07	<3.0	<1.5
PJ022634.0	0.64 ± 0.09	0.45 ± 0.07	0.71 ± 0.12	4.9 ± 0.9	17 ± 3.0
PJ030510.6	0.14 ± 0.02	0.20 ± 0.03	0.59 ± 0.10	5.0 ± 0.9	<2.0
PJ074852.6	0.22 ± 0.03	0.29 ± 0.05	1.00 ± 0.15	4.0 ± 0.9	5.6 ± 1.0
PJ084650.1	0.24 ± 0.03	0.31 ± 0.05	2.63 ± 0.40	17.2 ± 3.0	3.5 ± 0.5
PJ105322.6	0.19 ± 0.03	0.45 ± 0.05	0.43 ± 0.06	<5.6	<1.5
PJ112713.4	0.40 ± 0.06	0.56 ± 0.07	1.16 ± 0.15	2.86 ± 1.00	2.4 ± 0.4
PJ113805.5	0.14 ± 0.02	0.19 ± 0.02	<0.83	3.77 ± 1.00	1.5 ± 0.3
PJ113921.7	0.13 ± 0.02	0.19 ± 0.02	<1.25	<5.5	<0.5
PJ114038.5	1.00 ± 0.15	1.11 ± 0.20	12.5 ± 1.8	96.4 ± 15.0	17.6 ± 2.5
PJ114329.5	1.36 ± 0.19	1.25 ± 0.17	11.1 ± 1.5	16.6 ± 3.0	3.6 ± 1.0
PJ132217.5	0.34 ± 0.04	0.33 ± 0.05	<0.48	4.50 ± 1.50	1.5 ± 0.5
PJ132630.3	0.26 ± 0.03	0.25 ± 0.03	<1.3	<9.7	<0.5
PJ132934.2	0.37 ± 0.04	0.45 ± 0.05	0.71 ± 0.10	10.6 ± 2.0	3.6 ± 0.5
PJ133634.9	0.37 ± 0.06	0.33 ± 0.05	0.29 ± 0.10	3.63 ± 0.9	0.60 ± 0.15
PJ141230.5	0.22 ± 0.03	0.15 ± 0.03	0.55 ± 0.08	3.34 ± 0.7	1.5 ± 0.3
PJ144653.2	0.81 ± 0.08	0.79 ± 0.08	1.70 ± 0.20	7.4 ± 1.0	1.6 ± 0.3
PJ144958.6	0.35 ± 0.04	0.37 ± 0.04	0.28 ± 0.10	2.07 ± 0.63	1.3 ± 0.3
PJ154432.4	0.25 ± 0.03	0.17 ± 0.02	<0.69	2.3 ± 0.3	0.50 ± 0.15
PJ231356.6	0.53 ± 0.05	0.56 ± 0.06	0.49 ± 0.15	6.3 ± 1.3	4.48 ± 0.45

Downloaded from https://academic.oup.com/mnras/article/515/3/3911/6603847 by guest on 28 January 2026

Table 6. Best-fitting parameters of the starburst (SB) SED template and modified blackbody (BB) models for each source with derived dust and ISM masses.

Source ID	$\mu L_{\rm IR,SB}$[a] (10^{14} $L_\odot$)	$\mu SFR_{\rm SB}$ ($M_\odot$ yr^{-1})	$T_{\rm d}$ (K)	$\mu L_{\rm IR,BB}$[b] (10^{14} $L_\odot$)	$\mu SFR_{\rm BB}$ ($M_\odot$ yr^{-1})	$\mu M_{\rm d}$ (10^{10} $M_\odot$)	$\mu M_{\rm ISM}$ (10^{10} $M_\odot$)	$\mu_{\rm IR}$[c]
PJ011646.8	1.2 ± 0.3	9,001	–	–	–	2.08 ± 0.41	817 ± 162	7.0 ± 0.3 (1)
PJ014341.2	0.10 ± 0.02	1,064	$52.8^{+39.4}_{-14.6}$	0.10 ± 0.43	1064	0.12 ± 0.02	49 ± 9	7.1 ± 2.2 (1)
PJ022634.0	2.7 ± 0.6	23,147	–	–	–	2.77 ± 0.56	1074 ± 214	–
PJ030510.6	1.3 ± 0.2	12,715	–	–	–	1.51 ± 0.31	592 ± 119	2.2 ± 0.6 (1)
PJ074852.6	1.6 ± 0.3	13,806	–	–	–	1.81 ± 0.36	703 ± 140	–
PJ084650.1	1.1 ± 0.3	14,790	–	–	–	2.31 ± 0.46	908 ± 181	–
PJ105322.6	2.5 ± 0.5	16,735	$47.4^{+5.8}_{-6.2}$	2.24 ± 0.08	23 816	5.34 ± 1.07	2071 ± 414	7.6 ± 0.5 (2)
PJ112713.4	0.25 ± 0.04	1,845	–	–	–	0.41 ± 0.08	82 ± 16	–
PJ113805.5	0.24 ± 0.04	1,872	–	–	–	0.30 ± 0.06	119 ± 24	2.8 ± 0.4 (1)
PJ113921.7	1.2 ± 0.2	9,131	$47.4^{+3.6}_{-5.6}$	0.79 ± 0.13	8450	1.47 ± 0.30	576 ± 115	4.8 ± 0.4 (1)
PJ114038.5	0.026 ± 0.005	221	–	–	–	–	–	–
PJ114329.5	0.010 ± 0.003	81	–	–	–	–	–	–
PJ132217.5	1.2 ± 0.2	9,131	–	–	–	0.42 ± 0.08	163 ± 32	–
PJ132630.3	0.75 ± 0.16	4,677		0.56 ± 0.10	5982	0.83 ± 0.15	327 ± 65	4.3 ± 0.6 (1)
PJ132934.2	1.5 ± 0.3	12,028	–	–	–	1.63 ± 0.32	640 ± 128	11 ± 2 (3)
PJ133634.9	1.8 ± 0.4	17,944	–	–	–	1.74 ± 0.35	674 ± 135	–
PJ141230.5	3.1 ± 0.7	26,567	–	–	–	–	–	–
PJ144653.2	0.28 ± 0.07	1,910	–	–	–	0.53 ± 0.11	206 ± 41	3.9 ± 0.7 (1)
PJ144958.6	1.0 ± 0.2	8,821	–	–	–	1.17 ± 0.23	460 ± 92	10.1 ± 5.2 (1)
PJ154432.4	0.63 ± 0.13	5,261	$41.4^{+7.0}_{-4.2}$	0.50 ± 0.10	5332	0.97 ± 0.19	377 ± 75	14.7 ± 0.8 (2)
PJ231356.6	0.61 ± 0.13	6,383	–	–	–	0.75 ± 0.15	290 ± 58	6.1 ± 1.2 (1)

Notes. References: (1) Kamieneski et al. (in preparation); (2) Cañameras et al. (2018); (3) Díaz-Sánchez et al. (2017).
[a]$L_{\rm IR}$ is the FIR luminosity derived by integrating between 8 and 1000 μm in wavelength (Sanders & Mirabel 1996).
[b]The modified blackbody SED model used to derive $\mu L_{\rm IR,\,BB}$ is described in appendix C by Harrington et al. (2016).
[c]Magnification factor $\mu_{\rm IR}$ for dust or gas derived from lens modelling (see Section 5.1.2).

emission in galaxies. We adopt the functional form based on the derivation by Yun & Carilli (2002) for the modified blackbody model, and a detailed description of our method is given by Harrington et al. (2016) in appendix C. This approach was successful in deriving apparent IR luminosity and characteristic dust temperature for the eight *Planck* sources identified using the *Herschel* data studied by Harrington et al. (2016), yielding consistent estimates of IR luminosity and SFR as the template SED analysis.

Obtaining meaningful estimates of dust temperature $T_{\rm d}$ and IR luminosity is not as successful for those objects with only the *Planck* photometry. The primary reasons for this poor outcome are two-fold: (i) a low SNR of the *Planck* photometry, and (ii) the lack of constraints on the short wavelength side ($\lambda < 200$ μm) of the dust peak. Photometry along the Rayleigh–Jeans (R–J) part of the dust spectrum alone offers little constraints on $T_{\rm d}$ or the total IR luminosity. Even in cases where the *Planck* 857 GHz (350 μm) photometry probes the dust peak, a large uncertainty in the *absolute* photometry and the resulting low S/N ratio (e.g. $SNR \leq 3$, see Table 3) lead to poor constraints on $T_{\rm d}$ and $L_{\rm IR}$. In contrast, any available *Herschel* 250 μm photometry can provide a critical constraint on the dust peak, yielding a much stronger constraint on the dust SED, as shown by the magenta solid lines in Fig. 9.

For those sources with secure *Herschel* and AzTEC 1100 μm photometry, the derived $T_{\rm d}$ ranges between 41 and 53 K, with IR luminosity and SFR in good agreement with the results from the template SED analysis described in the next section. A more careful examination of Fig. 9 shows that the modified BB models fall slightly below the DSFG templates in the mid-IR range in nearly every case, reflecting the limitation of assuming a single temperature to characterize a dust SED, and the derived IR luminosity and SFR should be considered lower limits.

4.3 Template SED analysis

Even for an object without a strong constraint on the dust peak, IR luminosity and SFR can be estimated by adopting an SED, granted it is a plausible one for the object in consideration. There is growing evidence that SEDs of LIRGs vary with luminosity and redshift, but a remarkable similarity is also seen among objects of similar luminosity and SFR, even with the presence of an AGN (e.g. Kirkpatrick et al. 2012). For these *Planck*-selected DSFGs, template SEDs representing an ensemble of dust obscured young star clusters by Efstathiou et al. (2000) offer a good fit for the eight galaxies studied by Harrington et al. (2016), and we adopt the same SED templates here for the analysis of their IR luminosity and SFR.

As shown in Fig. 9, the template SEDs by Efstathiou et al. (2000) provide a good model for the observed SEDs of the 19 *Planck*-selected high-redshift sources as well from 1 μm to 20 cm, spanning 5 decades in wavelength. The photometric measurements in optical and near-IR bands are sometimes dominated by the foreground lensing galaxy or galaxies, and most of them are adequately modelled by adding a second SED component of an elliptical galaxy (Polletta et al. 2007). While these model SEDs are not perfect, they are sufficient to offer a good estimate of the apparent IR luminosity and SFR.

The apparent IR luminosity and SFR[11] derived from the template SED analysis are summarized in Table 6. They span the ranges (0.1–3.1) $\times$ 10^{14} $L_\odot$ and (1−27) $\times$ 10^3 $M_\odot$ yr^{-1}, respectively, for the 19 high-redshift sources analysed. For the five sources with *Herschel* photometry, the model SEDs and their derived quantities

[11]The SFRs in Table 6 are calculated using the empirical calibration by Kennicutt (1998), corrected for the Kroupa IMF [i.e. $SFR = L_{\rm IR}/(9.4 \times 10^9$ $L_\odot)$ $M_\odot$ yr^{-1}].

Downloaded from https://academic.oup.com/mnras/article/515/3/3911/6603847 by guest on 28 January 2026

(IR luminosity and SFR) are in good agreement between the modified blackbody modelling and the template SED analysis.

The radio continuum portion of the template SEDs shown in Fig. 9 is a model extension of the dusty starburst SEDs by Efstathiou et al. (2000) using the radio–IR correlation (see review by Condon 1992; Yun & Carilli 2002). Over 98 per cent of the local SFGs selected in the IR follow this relation closely (Yun, Reddy & Condon 2001), and the majority of these *Planck*-selected DSFGs also show 20 cm radio continuum detection or upper limits that are consistent with the local relation. Yun et al. (2001) have also shown that about 1 per cent of local SFGs are a factor of a few to 10 times brighter in radio continuum than the expected relation, indicating the presence of a weak radio AGN activity, and this fraction rises to 10 per cent for $L_{\rm IR} \gtrsim 10^{11}$ L$_\odot$. A few *Planck*-selected sources (PJ022633.9, PJ074852.6, and PJ231356.6) show a similar radio-excess with 3–10 times stronger radio continuum, indicating a possible presence of a weak radio AGN. These sources show remarkably little sign of any AGN activity (see Section 5.1.1), and this radio-excess might be the only clue that some of these sources might be hosting a heavily obscured AGN (also see Geach et al. 2015). Our high-resolution radio continuum imaging study using the VLA has shown, however, that the excess radio continuum is associated with the nuclei of the foreground lensing galaxy, rather than the submillimetre source, at least in some of the cases (Kamieneski et al., in preparation).

5 DISCUSSION

5.1 Extreme IR luminosity of Planck DSFGs

Harrington et al. (2016) have found their eight high-redshift *Planck* sources identified using archival *Herschel* data are among the most luminous IR sources known, with apparent IR luminosity $L_{8-1000\mu} \geq 10^{14}$ L$_\odot$ in the majority of the cases (also see Cañameras et al. 2015). They match or exceed the IR luminosities of the *WISE*-selected HyLIRGs, which are the most LIRG population previously identified (Tsai et al. 2015). When the 19 new high-redshift *Planck* sources from this study are added, as shown in Fig. 10, it becomes clearer that the *Planck*-selected DSFGs overlap broadly with the *Herschel*, *WISE*, *ACT*, and *SPT*-selected DSFGs in their apparent IR luminosity, but they occupy the top range in $L_{\rm IR}$ at each redshift range out to $z \approx 4$. The majority of the *Planck*-selected DSFGs cluster above $L_{\rm IR} \gtrsim 10^{14}$ L$_\odot$, and the *Planck*-selected DSFGs are in fact the dominant population (17 out of 25, or 68 per cent) among all known objects with $L_{\rm IR} \gtrsim 10^{14}$ L$_\odot$. Adding the latest compilations of the *SPT* (Reuter et al. 2020), *ACT* (Su et al. 2017; Gralla et al. 2020), and *Herschel* (Bussmann et al. 2013; Wardlow et al. 2013; Bakx et al. 2018) sources in the comparison makes it even clearer that these *Planck*-selected DSFGs are on average 4–10 times more luminous than the lensed DSFGs identified by the other surveys. The lensed $z = 3.91$ QSO APM 08279+5255[12] (Irwin et al. 1998; Weiß et al. 2007) stands out as a true exception in this comparison.

The *ACT* and *SPT* sources extend out to a higher redshift of $z \sim 6$ while no *Planck* source is identified at $z > 4$ yet. This is likely reflecting the redshift bias in the sample selection: *Planck* and *Herschel* sources are selected primarily at 857 and 545 GHz bands and are thus preferentially at lower redshifts compared with *ACT* and *SPT* sources selected at 220 and 150 GHz (see Béthermin et al. 2015 and Casey et al. 2018 for discussions about the selection effects imposed by wavelength selection). The $z \geq 4$ luminous DSFG population is also rarer in number, and a larger survey is needed to find them. Our redshift survey of the full sample of the *Planck*-selected sources and analysis of their physical properties should reveal whether the *Planck* and other surveys probe the same parent population.

[12]Detailed modelling of dust continuum and warm molecular gas emission by Weiß et al. (2007) suggests that the bulk of its bolometric luminosity arises from a compact (100–350 pc) radius region surrounding the AGN, which is magnified by an effective magnification of 60–120.

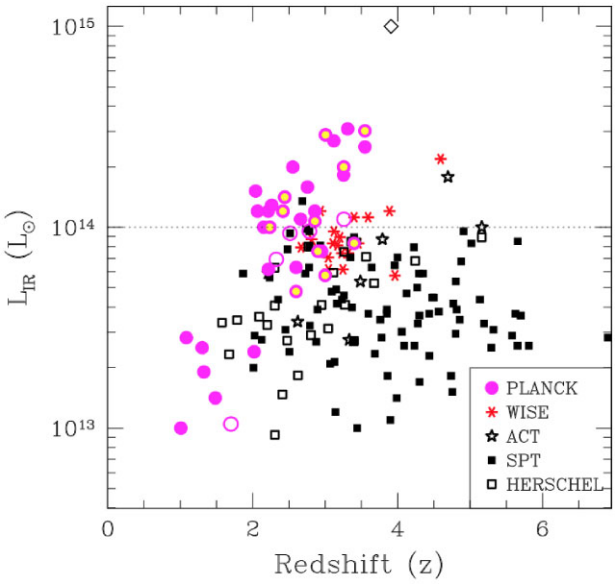

Figure 10. Comparison of IR (8–1000 μm) luminosity of the *Planck* sources (filled magenta circles, from this study as well as by Cañameras et al. 2015; Harrington et al. 2016) with those of strongly lensed SMGs identified by the *SPT* (Vieira et al. 2013; Weiß et al. 2013; Reuter et al. 2020), *ACT* (Su et al. 2017; Gralla et al. 2020), and the *Herschel* (Bussmann et al. 2013; Wardlow et al. 2013; Bakx et al. 2018). The four *Planck–WISE* sources previously identified as luminous DSFGs are shown with empty magenta circles while those identified previously by Cañameras et al. (2015) are shown by thicker circle filled with a yellow dot. The most luminous *WISE* sources (Tsai et al. 2015) are shown as stars, while the $z = 3.91$ lensed IR QSO APM 08279+5255 (Irwin et al. 1998; Rowan-Robinson 2000), the most luminous object known in the IR, is shown as a diamond. Seventeen out of the 25 most luminous known IR sources in the entire sky are from our survey.

There is a second grouping of *Planck*-selected DSFGs in the redshift range of $z = 1$–2 with $L_{\rm IR} \geq 10^{13}$ L$_\odot$. While they are not as luminous as many of the $z > 2$ DSFGs shown in Fig. 10, they are still some of the most luminous galaxies known at $z < 2$. The *absence* of DSFGs with $L_{\rm IR} \geq 10^{14}$ L$_\odot$ in the same redshift range is noteworthy. A flux-limited survey such as this is generally not biased against bright objects, and our *Planck* colour selection (see Section 2.1.2) is designed to ensure a detection if they exist. Gravitational lensing can introduce an element of a bias against nearby objects because a massive foreground object is required for strong gravitational lensing. The magnitude of this effect is heavily dependent on assumptions going into computing a lensing optical depth, as shown by the broad range of predictions by Blain (1998b), Hezaveh & Holder (2011), Béthermin et al. (2015), and Strandet et al. (2016). The fraction of *Planck*-selected lensed DSFGs in the redshift range $z = 1$–2 is ≈20 per cent of the total, nearly identical to that of the *Herschel*-selected DSFGs (Amvrosiadis et al. 2018). If the two $z = 1$ sources with a single line redshift are actually $z = 2$ sources (see Table 4), then the source fraction is reduced to ≈15 per cent of the total.

Another possibility is that DSFGs with $L_{\rm IR} \geq 10^{14}$ L$_\odot$ are too rare to be found in the volume of the lower redshift range. The co-

Downloaded from https://academic.oup.com/mnras/article/515/3/3911/6603847 by guest on 28 January 2026

moving volume of the redshift range between $z = 1$ and $z = 2$ is about 30 per cent of the entire co-moving volume enclosed within $z = 4$, and one can expect approximately seven DSFGs with $L_{\rm IR} \geq 10^{14}$ L$_\odot$ in our sample between $z = 1$ and $z = 2$ if they occur with the same spatial density. While a small sample size prevents us from drawing a firm conclusion, this analysis suggests that these extreme luminosity DSFGs are indeed absent during the past 10 Gyr of the cosmic history, in line with the known decline in the cosmic SFR density between $z = 2$ and now (Madau & Dickinson 2014; Scoville et al. 2017; Zavala et al. 2021).

So, what exactly are these extremely luminous DSFGs identified by the *Planck* survey? Modelling of the extragalactic millimetre and submillimetre source populations such as by Blain (1998b) and Negrello et al. (2007) has suggested that a strongly lensed population of high-redshift DSFGs would dominate the bright end of the source counts. On the other hand, the most luminous high-redshift objects discovered by previous all-sky IR surveys such as APM 08279+5255 (Irwin et al. 1998), FSC 10214+4724 (Rowan-Robinson et al. 1991), and H1413+117 (Barvainis, Antonucci & Coleman 1992) are all IR QSOs, as are the more recently discovered population of extremely luminous IR sources by the *WISE* survey (Tsai et al. 2015). Therefore, there are at least two different potential explanations for the extreme apparent luminosity of these *Planck*-selected high-redshift sources, and we explore these scenarios further here.

5.1.1 IR QSO scenario

There are at least two different potential sources of luminosity for these extreme luminosity objects: (i) a massive starburst powered by young stars and (ii) an accreting SMBH. Both processes might be at work simultaneously in almost all cases at some level, and either process might dominate the radiative output of a galaxy at any given time. The luminosity of a starburst produced by OB stars averaged over their main-sequence (MS) lifetime yields:

$$L_{\rm SB} = 4.9 \times 10^{43} \left[\frac{\dot{M}}{\rm M_\odot\ yr^{-1}}\right]\ {\rm erg\ s^{-1}}, \quad (1)$$

where $\dot{M}$ is the gas consumption rate by SF (see equation 5 by Scoville & Young 1983). If only the luminosity and lifetime of O stars are considered, time-averaged $L_{\rm SB}$ can be ∼5 times larger (N. Scoville, private communication). In comparison, accretion luminosity of an SMBH is

$$L_{\rm BH} = \epsilon \dot{M} c^2 = 6 \times 10^{45} \left[\frac{\epsilon}{0.1}\right] \left[\frac{\dot{M}}{\rm M_\odot\ yr^{-1}}\right]\ {\rm erg\ s^{-1}}, \quad (2)$$

where ϵ is the radiative efficiency and $\dot{M}$ is the mass accretion rate. Therefore, an accreting BH can produce luminosity 20–100 times more efficient than a starburst at any stage. On the other hand, BH accretion is spatially limited to the parsec-scale immediate sphere of influence, while a starburst can occur over 100s of parsec to several kiloparsec regions simultaneously. As a result, detailed numerical modelling of a rapidly accreting BH within a merger-driven starburst, such as by Hopkins et al. (2006, 2008), have shown that the peak luminosity of a starburst and that of an SMBH fuelled by the same inflowing gas streams are comparable in magnitude, and some care might be needed to distinguish their respective luminosity contributions.

The most luminous IR sources with $L_{\rm IR} \gtrsim 10^{14}$ L$_\odot$ known prior to the discovery of these *Planck*-selected DSFGs were all IR QSOs, whereas a galaxy undergoing SF has a plausible physical upper limit of $L_{\rm IR} \approx (2-3) \times 10^{13}$ L$_\odot$ ($SFR \approx 2000-3000$ M$_\odot$ yr^{-1}, see

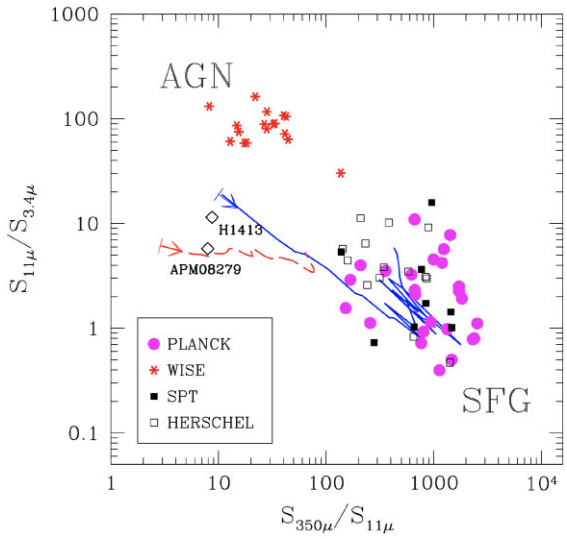

Figure 11. Mid-IR to FIR colour diagnostic plot for star-forming and AGN galaxies. This is essentially the same plot as fig. 9 by Harrington et al. (2016) but including all *Planck*-selected high-redshift sources and using the 350–11 μm colour for the *x*-axis. All symbols are the same as Fig. 10. Colour tracks for the $z = 2$ SF template (solid blue line) and the featureless power-law AGN template (long dashed red line) by Kirkpatrick et al. (2013) are shown, starting from $z = 0.5$ and ending at $z = 4$, as marked by the arrows. The high-redshift IR QSOs APM 08279+5255 (Irwin et al. 1998) and H1413+117 (Barvainis et al. 1992) are also shown for reference.

Harrington et al. 2016). Since an accreting BH can be highly efficient in converting mass to luminosity, a heavily obscured luminous AGN activity can offer a natural explanation for these *Planck*-selected DSFGs with $L_{\rm IR} \gtrsim 10^{14}$ L$_\odot$, as is the case for the *WISE* HyLIRGs (Tsai et al. 2015). A merger-driven starburst and subsequent, or simultaneous, fuelling of a luminous AGN has been suggested as a natural explanation for the high frequency of ULIRGs with warm IR colour and Seyfert spectra (Sanders et al. 1988). Numerical simulations of this scenario (Hopkins et al. 2006, 2008) have yielded a plausible cosmological framework for the connection between gas-rich galaxy mergers and quasar activity. This mechanism also serves as the prototype of the BH-host coevolution driven by quasar-mode feedback (see review by Kormendy & Ho 2013).

The mid-IR to FIR colour diagnostic analysis for IR AGNs first introduced by Kirkpatrick et al. (2012) was later adopted for the *WISE* bands by Harrington et al. (2016) to explore the frequency of IR QSOs among the *Planck*-selected DSFGs. The same analysis repeated with better statistics in Fig. 11, and we find that *all* of our *Planck*-selected DSFGs have a cold IR SED of SFGs with little evidence for any enhanced mid-IR warm dust emission characteristic of an enshrouded AGN activity. The individual SEDs shown in Fig. 9 also support this conclusion, although *WISE* 11 and 22 μm bands are the only measurements sensitive to the power-law IR AGN emission. This is a rather surprising and somewhat unexpected outcome, given their remarkable luminosity and the widely adopted merger-driven starburst-AGN co-evolution model (Hopkins et al. 2006, 2008). In fact, one of the key predictions of the AGN co-evolution model is that up to 90 per cent of the luminous quasar phase, fuelled by the high gas accretion that also powers the starburst, should remain obscured by dust, presumably leading to their identification as IR QSOs such as APM 08279+5255 or as power-law mid-IR sources such as the *WISE*-selected HyLIRGs found on the top-left corner of Fig. 11.

Downloaded from https://academic.oup.com/mnras/article/515/3/3911/6603847 by guest on 28 January 2026

A generic feature in these models is a 10–20 Myr delay between the peak starburst and the start of the quasar phase (e.g. see fig. 1 by Hopkins et al. 2008), and one possible explanation is that these *Planck*-selected DSFGs are seen exclusively during this brief phase prior to the quasar phase. On the other hand, this time-scale is an order of magnitude shorter than the gas depletion time-scale and the UV/optical radiation lifetime for a simple stellar population responsible for dust heating, and objects in this phase should be 10 times rarer than the objects in the AGN phase if one were to take this model results literally. A large fraction of these DSFGs might contain a luminous AGN if this SB–AGN co-evolution scenario occurs ubiquitously. The *WISE*-selected HyLIRGs are largely distinct from the *Planck* DSFGs in Fig. 11, and a simplistic interpretation of the co-evolution scenario is not supported by these data.

Drawing a parallel to the X-ray regime, one possible explanation is that the 'quasar activity' associated with these *Planck* DSFGs is so deeply embedded in dust that little or no activity is visible even at mid-IR to FIR range ($N_{\rm H} \gg 10^{24\text{–}25}$ cm^{-2}, see Draine 1989), with uniform and complete blockage of light. Since AGN activity is likely limited to the central several parsec region, it might require just one well-placed dense gas/dust clump to hide the luminous activity.

Neither the *Planck* selection nor the *WISE* selection is finding many objects bridging the gap between the AGN and DSFGs in Fig. 11. This might be an important clue if the popular co-evolution model applies to these HyLIRG populations. The one object falling in the bridge region, W1026−0529, was initially reported as a $z \sim 3$ HyLIRG by Tsai et al. (2015) and has a substantial AGN and cold dust components in its SED. However, it was recently shown to be a lower redshift ($z = 0.82$) source with a much lower IR luminosity ($L_{\rm IR} \sim 10^{13}$ L$_\odot$, Penney et al. 2020), and this might be a misplaced object in this comparison. The *WISE*-selected HyLIRGs are on average ∼3 times fainter than the *Planck*-selected DSFGs, and one possible way to connect them in the co-evolution scenario is that the AGN-dominated *WISE* sources are seen after much of the starburst activity has shutdown. This scenario is also consistent with the average gas column densities of $N_{\rm H} \approx 10^{23\text{–}24}$ cm^{-2} inferred from the measured extinction for the *WISE*-selected HyLIRGs by Assef et al. (2015). This is more than 10 times greater absorption than the typical dividing line between Type 1 and Type 2 AGN, but it is still 10 times less than the gas column required to hide the AGN completely in the IR. The Eddington ratios for their mass accretion rates derived by Wu et al. (2018) are close to unity, suggesting that they represent a transitional, high accretion phase between obscured and unobscured quasars, as expected in the later stages in the co-evolution scenario.

In summary, these extremely luminous IR sources without any visible signs of quasar activity seem to be the norm, rather than exceptions, among the 31 *Planck*-selected DSFGs. This result contrasts with the theoretical expectation from the popular starburst–AGN co-evolution and quasar-mode feedback scenario by Hopkins et al. (2006, 2008) and the observational trend of a higher AGN fraction among DSFGs with increasing luminosity ($L_{\rm IR} \geq 10^{11\text{–}12}$ L$_\odot$; e.g. Treister et al. 2010). The correction for lensing amplification should lower the intrinsic luminosity of these *Planck* DSFGs by an order of magnitude or more (see next section), but the absence of evidence for an accreting AGN in the IR is still unexpected. An additional factor, such as an extreme opacity with $N_{\rm H} \gtrsim 10^{24}$ cm^{-2}, is needed to bridge the gap between the model and the data. Future observations at wavelengths between 50 and 100 μm and hard X-ray observations at ≥30–100 keV energy or a reflected component (e.g. Fe K line, Teng et al. 2009) are crucial for setting strong constraints on any energetic contribution by a deeply embedded AGN.

5.1.2 *Strong gravitational lensing*

SF is a self-regulated process where gas supply is modulated by the mechanical and radiative feedback from young stars. In the most extreme starbursts, radiation pressure can limit the luminosity density and SF density to $\sim 10^{13}$ L$_\odot$ kpc^{-2} and $\sim 10^{3}$ M$_\odot$ yr^{-1} kpc^{-2}, respectively (Thompson, Quataert & Murray 2005). Such 'Eddington-limited' starburst conditions are observed in local ULIRGs with $L_{\rm IR} \gtrsim 10^{12}$ L$_\odot$ but limited only to their central 100 pc regions. In more extreme high-redshift SMGs with $L_{\rm IR} \gtrsim 10^{13}$ L$_\odot$, multiple such regions are found embedded in a more diffuse, kiloparsec-scale structure (e.g. Iono et al. 2016; Tadaki et al. 2018). An even more luminous object with $L_{\rm IR} \gtrsim 10^{14}$ L$_\odot$ would require a correspondingly larger gas/SB structure spanning at least several to 10 kpc in size and an even larger cold gas reserve ($M_{\rm ISM} \gtrsim 10^{12}$ M$_\odot$) and gas inflow rate ($\dot{M}_{\rm gas} \gtrsim 10^{4}$ M$_\odot$ yr^{-1}).

Gravitationally lensed objects are common at the bright end of the submillimetre source counts (e.g. Blain 1998a, b; Negrello et al. 2010). Strong lensing is likely important for these *Planck*-selected sources as well, and the ALMA and *HST* images of the 12 new *Planck* sources shown in Fig. 7 clearly support the lensing hypothesis with their characteristic Einstein ring or arc morphology (see Section 3.3). The angular extent of the submillimetre continuum and stellar light ranges between 1 and 10 arcsec, making them some of the largest Einstein rings or arcs ever found (Lowenthal et al., in preparation – also see Frye et al. 2019). They are fully resolved by the *HST* ($\theta \approx 0.1$ arcsec) and the ALMA ($\theta \approx 0.4$ arcsec) in almost all cases. A detailed discussion of lensing models and interpretations requires a significant amount of additional data and extensive technical descriptions, and they will be presented elsewhere (Kamieneski et al., in preparation).

The total magnification for the IR continuum $\mu_{\rm IR}$ derived from the ALMA 260 GHz continuum images ranges between 2.2 and 14.7 (a median value of ∼7) for the *Planck*-selected DSFGs with high-resolution ALMA data (see Table 6 and Fig. 12). Dust continuum imaged by the ALMA corresponds to a rest-frame wavelength of 350 μm at $z = 2$, and the derived $\mu_{\rm IR}$ values are reasonable estimates of the total magnification factor for their IR luminosity and gas mass. They are similar to the range of total magnification derived for the strongly lensed DSFGs selected in the rest-frame IR by *Herschel* and *SPT* surveys (Bussmann et al. 2013, 2015; Dye et al. 2015, 2018; Rybak et al. 2015; Spilker et al. 2016; Massardi et al. 2018). The lensing magnification derived for some of the *SPT*-selected sources by Spilker et al. (2016) are slightly larger in comparison, and this likely reflects some systematic differences in model assumptions or input data. For example, Enia et al. (2018) and others have found that extended sources with multiple emission components lead to a lower magnification while a bright, compact emitting region can be magnified by a larger factor.

A comparison of apparent total IR luminosity as a function of their total lensing magnification factor $\mu_{\rm IR}$ shown in Fig. 12 indicates that the *Planck*-selected DSFGs have 3–10 times higher apparent IR luminosity because their *intrinsic* luminosity is larger. With the exception of 1 or 2 sources, nearly all of the *Planck*-selected DSFGs lie along or above the long solid line representing a DSFG with an intrinsic luminosity $L_{\rm IR} = 10^{13}$ L$_\odot$. A natural explanation is that the *Planck*-selected DSFGs are the examples of strongly lensed DSFGs at the tip of their luminosity function while the majority of the *Herschel*- and *SPT*-lensed DSFGs represent the more numerous, lower luminosity sources with $(1\text{–}3) \times 10^{12}$ L$_\odot$.

Whether these *Planck*-selected DSFGs are simply the most luminous but otherwise ordinary examples of the known population of DSFGs or something entirely different remains an interesting

Downloaded from https://academic.oup.com/mnras/article/515/3/3911/6603847 by guest on 28 January 2026

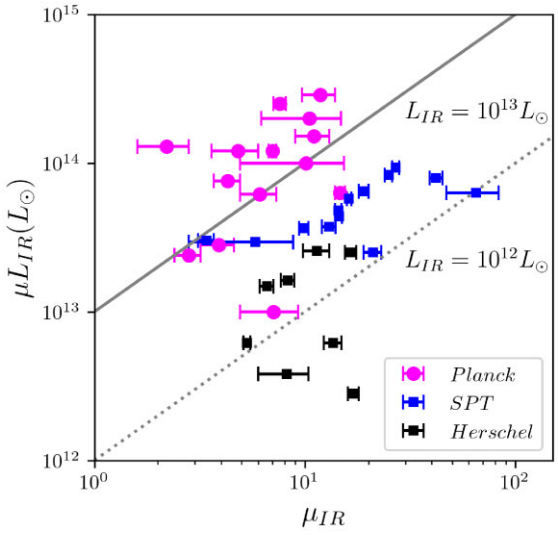

Figure 12. Apparent IR luminosity of the *Planck*, *Herschel*, and *SPT*-selected lensed DSFGs as a function of their total lensing magnification $\mu_{\rm IR}$. The total magnification factors derived from detailed gravitational lens modelling are shown in magenta filled circles (see Table 6), and they are compared with equivalent quantities for *Herschel* and *SPT*-selected lensed DSFGs (shown in filled squares) by Bussmann et al. (2013,2015), Dye et al. (2015, 2018), Rybak et al. (2015), Spilker et al. (2016), and Massardi et al. (2018). The dotted and solid lines represent a source with intrinsic IR luminosity of $L_{\rm IR} = 10^{12}$ L$_\odot$ and 10^{12} L$_\odot$, respectively.

question. By adopting a source count model for the unlensed FIR or submillimetre source population and a distribution of lensing optical depth computed from a halo mass function, one can predict the frequency of extremely bright DSFG population, as was done by Blain (1998a, b) and Negrello et al. (2010). For example, fig. 1 by Negrello et al. (2010) shows that all sources brighter than 100 mJy at 500 μm wavelength band should be strongly lensed versions of otherwise normal background DSFGs. At the integrated source density of 0.01 deg^{-2} for the *Planck* DSFGs, even the strongly lensed DSFG population is expected to decrease rapidly as it approaches the 300 mJy level according to this model. In comparison, the majority of the 500 μm flux densities of the 24 *Planck* DSFGs listed in Table 3 are larger than 300 mJy, with a median of 426 mJy. Noise bias and source blending can lead to an overestimate of flux density, and two sources (Cosmic Eyelash and PJ090403.9) are associated with significantly higher PCCS flux density compared with their *Herschel*/SPIRE 500 μm photometry among the sources with both *Planck* and *Herschel* measurements. On the other hand, the remaining five out of seven sources show consistent photometry, and their *Herschel*/SPIRE 500 μm flux density (341–771 mJy) exceeds the model prediction. This apparent discrepancy might not be hugely significant as the details of these predictions depend on the precise modelling of the lensing optical depth (Blain 1998a, b). Finding a significant number of new sources with exceedingly bright submillimetre continuum in our ongoing follow-up study may require a new analysis of the lensing statistics and the nature of the DSFG population.

5.2 Gas mass and consumption time

Since the amount of total cold gas is one of the key drivers for the SFR in individual galaxies ('Kennicutt–Schmidt Law') and for the cosmic SF density evolution (e.g. Yun et al. 2009; Walter et al. 2014; Scoville et al. 2017), methods to determine cold gas masses of distant galaxies are subjects to continued research and improvement. Detecting gas mass tracers such as CO lines and dust continuum with sufficient S/N ratios is difficult and time-consuming for high-redshift systems, and both the measurements and their gas mass calibrations are frequently subject to large uncertainties.

The CO lines and dust continuum associated with the *Planck*-selected DSFGs reported here and by Cañameras et al. (2015) and Harrington et al. (2016) are significantly brighter than the most systems studied at similar redshifts previously, and the resulting high S/N measurements enable highly reliable and consistent gas mass estimates (see Harrington et al. 2021 for a more complete review of this topic). With this improved sense of reliability, we can examine their gas consumption times and compared with them with those of other populations of high-redshift DSFGs.

5.2.1 *Gas mass estimates from CO lines*

One or more CO lines detected by the RSR for the 24 *Planck*-selected sources listed in Table 4 can yield a redshift and line luminosity $L'_{\rm CO}$ for each line detected, and this CO line luminosity can be used to estimate the total molecular gas mass $M_{\rm H2}$ by adopting a set of standard assumptions as described in Section 3.2. A major uncertainty in this gas mass calibration due to gas excitation can be directly addressed by measuring the full CO rotational ladder and analysing the data using a detailed radiative transfer model. To address this issue, we have recently conducted a survey of the CO rotational transitions and [C I] lines for a sample of 24 *Planck*-selected DSFGs (including the 16 sources discussed in this paper) using the *GBT*, *IRAM* 30 m telescope, and the *APEX* telescope (Harrington et al. 2021). A total of 160 CO lines and 37 [C I] lines are analysed to derive gas excitation and bulk properties using two different non-LTE radiative transfer models. The radiative transfer model assuming a turbulence driven lognormal gas density distribution that simultaneously fits the CO and [C I] lines as well as the dust continuum is new and one of the most innovative models to date, and readers are invited to examine that paper for important technical details. The total molecular gas masses derived from this analysis are shown as '$M_{\rm gas}$' in Table 4. The data and the analysis presented by Harrington et al. confirm that the CO line excitation, even when measured with a high SNR ($\gtrsim$10–20), can vary considerably among different galaxies.

A comparison of the total molecular gas masses derived from the multitransition data using a full radiative transfer model ($M_{\rm gas}$, Harrington et al. 2021) with the molecular gas masses derived from the RSR-derived CO line luminosity ($M_{\rm H2}$, see Section 3.2) is shown in Fig. 13. The agreement between $M_{\rm gas}$ and $M_{\rm H2}$ is very good on average with a median ratio of $M_{\rm gas}/M_{\rm H2} \approx 0.9$ (with a scatter of 0.35 dex). Harrington et al. (2021) found an average $<\alpha_{\rm CO}>$ value of 3.4 $\pm$ 2.1, with a mean value of 4.2 for the galaxies with the best dust photometry and CO/[CI] line coverage, and this is very close to our adopted value of 4.3 (Bolatto et al. 2013) for the analysis of the RSR data. This explains the good agreement between the two derived molecular gas mass estimates and much of the scatter in the measured gas mass ratios. The uncertainty in the line excitation as well as the source-to-source variation likely dominates the scatter in the derived mass ratios. This comparison suggests that molecular gas masses derived from a single CO line adopting the standard assumptions (Section 3.2) are generally reliable, although any individual estimate may be off by a factor of 2 or more (see fig. 13 by Harrington et al. 2021).

Downloaded from https://academic.oup.com/mnras/article/515/3/3911/6603847 by guest on 28 January 2026

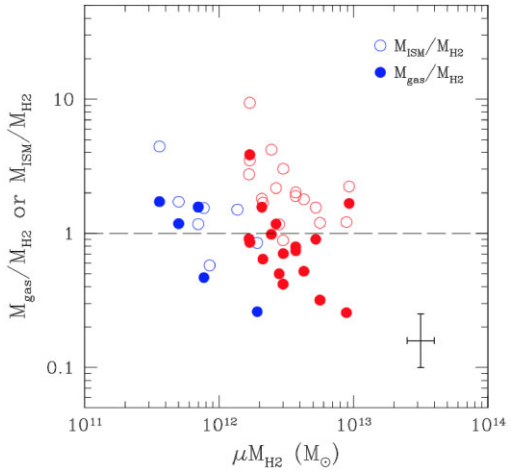

Figure 13. Comparison of total molecular gas mass derived from the multi-transition data using the full radiative transfer model ($M_{\rm gas}$, Harrington et al. 2021), $M_{\rm ISM}$ (gas mass derived from 1 mm continuum), and $M_{\rm H2}$ (molecular gas mass derived from RSR derived CO line luminosity). The molecular gas mass $\mu M_{\rm H2}$ shown on the x-axis is the apparent gas mass without correcting for the magnification factor (not known yet in all cases). Red and blue symbols represent $M_{\rm H2}$ masses derived from CO (3–2) and CO (2–1) line, respectively. The long dashed line marks the '$M_{\rm ISM}/M_{\rm H2} = 1$' relation, indicating the one-to-one correspondence between the ISM mass and the CO-derived molecular gas mass. The error bar shown on the bottom-right corner illustrates the typical measurement uncertainty associated with these quantities.

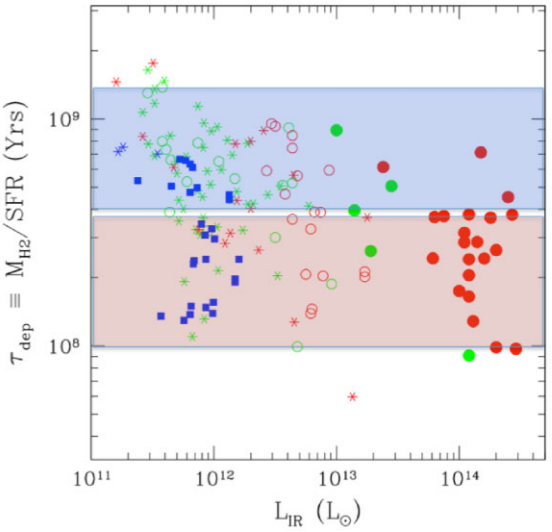

Figure 14. Comparison of gas depletion time $\tau_{\rm dep} \equiv M_{\rm H2}/SFR$ as a function of apparent IR luminosity. *Planck*-selected sources are shown as filled green ($z < 2$) and red ($z \geq 2$) circles. They are compared with representative samples of stellar mass-selected 'MS' SFGs (stars; Magdis et al. 2012; Tacconi et al. 2013), submillimetre-/IR-selected starbursts (SMGs, in empty circles; Magnelli et al. 2012), and $z = 0$ IR luminous galaxies (LIRGs/ULIRGs, in blue squares; Chung et al. 2009). The red and blue shaded regions mark the mean ranges of $\tau_{\rm dep}$ for galaxies on the star-forming MS galaxies and starburst galaxies with 10 times the SFR for a characteristic stellar mass of 5×10^{10} M$_\odot$ (see fig. 10 by Scoville et al. 2017).

5.2.2 *Gas mass estimates from 1 mm continuum*

The total dust mass $M_{\rm d}$ and the 'ISM mass' $M_{\rm ISM}$ derived from the observed 1.1 mm AzTEC photometry or ALMA 260 GHz photometry for assumed dust temperature of $T_{\rm d} = 25$ K are listed in the last two columns of Table 6. The ISM mass $M_{\rm ISM}$ is derived from the empirical relation between the optically thin dust continuum in the R–J regime and total cold gas mass through an empirical calibration of total gas-to-dust mass ratio (Scoville et al. 2016, 2017):

$$M_{\rm ISM}({\rm M}_\odot) = \frac{1.78\times10^4 D_{\rm L}^2}{(1+z)^{4.8}} \left[\frac{S_{\nu,{\rm obs}}}{\rm mJy}\right] \left[\frac{353\,{\rm GHz}}{\nu_{\rm obs}}\right]^{3.8} \left[\frac{\Gamma_0}{\Gamma_{\rm RJ}}\right], \quad (3)$$

where $D_{\rm L}$ is the luminosity distance in megaparsec, $S_{\nu,\,{\rm obs}}$ is the measured flux density in mJy (for $\lambda_{\rm rest} \geq 250$ μm), and the last term is the R–J correction factor. We adopt the same dust emissivity $\beta = 1.8$ to be consistent with the Scoville et al. derivation.

This total ISM mass $M_{\rm ISM}$ is a widely used quantity because 1 mm continuum is much easier and faster to measure using the ALMA or a broad-band photometer such as AzTEC, compared with CO line measurements. However, $M_{\rm ISM}$ is also subject to systematic uncertainties depending on adopted $T_{\rm d}$ and β, as well as CO and dust abundances. A comparison of the total ISM mass ($M_{\rm ISM}$) with the molecular gas mass derived from CO line luminosity ($M_{\rm H2}$) in Fig. 13 shows that the ISM masses derived from the 1 mm dust continuum are systematically larger with a median ratio of $M_{\rm ISM}/M_{\rm H2} \approx 1.5$ ($\sigma = 0.15$ in dex), nearly independent of the apparent gas mass.

One plausible explanation for this systematic difference is that the CO to H_2 conversion relation used: The value Scoville et al. adopted is 50 per cent larger than the $\alpha_{\rm CO}$ we adopted from Bolatto et al. (2013).[13] However, this is only a part of the complete story. For example, $M_{\rm ISM} \equiv M_{\rm HI} + M_{\rm H2}$ includes both *atomic* and molecular gas masses and is always expected to be larger than $M_{\rm H2}$ alone. The molecular gas mass fraction is expected to be near unity among these massive gas-rich galaxies (Scoville et al. 2017), unlike in the local late-type galaxies where $M_{\rm HI}$ dominates the gas mass (e.g. Keres et al. 2005). Similarly, adopting dust temperature of $T_{\rm d} = 35$ K (might be appropriate for gas/dust heated by an intense starburst) instead of the mass-weighted dust temperature $T_{\rm d} = 25$ K, the derived $M_{\rm ISM}$ drops by a factor ≈2 (Harrington et al. 2016). The comparison of different gas mass estimates shown in Fig. 13 suggests that there is a *systematic* uncertainty of order 50 per cent in total gas masses estimated using the different methods.

5.2.3 *Gas consumption/depletion time*

The gas depletion times $\tau_{\rm dep}$ ($\equiv M_{\rm H2}/SFR$)[14] for the *Planck*-selected DSFGs are shown in Fig. 14, and they cover the same range as those of the unlensed DSFGs and star-forming MS galaxies studied by Magnelli et al. (2012), Magdis et al. (2012), and Tacconi et al. (2013) – also, see the review by Tacconi, Genzel & Sternberg (2020). This may indicate that they share the same underlying physical processes that drive and regulate SF in these galaxies, despite their 10 to 100 times larger apparent IR luminosity. A more detailed comparison with the ranges of $\tau_{\rm dep}$ characterizing the MS SFGs and starburst galaxies at $z = 1$–4 (shaded regions in Fig. 14) suggests that these *Planck*-selected DSFGs mostly show gas depletion times more characteristic of a starburst population [$\tau_{\rm dep} = (1\text{–}3) \times 10^8$ yr,

[13] See Scoville et al. (2016) for a detailed recent review of this CO to H_2 conversion factor.

[14] Gas depletion time is defined as $\tau_{\rm dep} \equiv \frac{1}{2} M_{\rm H2}/SFR$ in some papers, assuming 1/2 of the gas is lost to feedback/outflow, but we ignore this order unity coefficient since the coupling efficiency between feedback and ISM is poorly understood.

Downloaded from https://academic.oup.com/mnras/article/515/3/3911/6603847 by guest on 28 January 2026

similar to the local ULIRGs, Chung et al. 2009] than the star-forming 'MS' population. Accounting for the magnification factor of $\mu \sim 10$, the intrinsic IR luminosities of these *Planck*-selected DSFGs (1–3 $\times$ 10^{13} $L_{\odot}$, see Fig. 12) are near the top end of the IR luminosity of the submillimetre-/IR-selected DSFGs studied by Magdis et al. (2012) and others, and their gas consumption times also agree well.

The similar gas depletion times derived for the *Planck*-selected DSFGs with those of the local ULIRGs and high-redshift DSFGs has several interesting implications. Firstly, this result indicates that differential magnification associated with lensing does not play a significant role here. In theory, CO and dust continuum emission could be amplified by different amounts and could lead to a larger scatter in $\tau_{\rm dep} \equiv M_{\rm H2}/SFR$. The observed scatter is similar to or tighter than those of the unlensed galaxies, and this might be a natural consequence of lensing magnifying areas larger than the spatial scale where the correlation between SF and gas density is known to hold (0.5–1 kpc; see Schinnerer et al. 2019, and references therein). This comparison also supports the claim by Scoville et al. (2017) that the lack of dependence of SF efficiency ($1/\tau_{\rm dep}$) on galaxy mass is the result of SF process dictated by the internal structure of the GMCs, rather than global galaxy properties. Additionally, this comparison also supports the absence of a substantial AGN contribution to the IR luminosity for these *Planck*-selected DSFGs discussed in Section 5.1.1, as any significant IR luminosity by a dust obscured AGN would lead to an overestimate of SFR and correspondingly shortened $\tau_{\rm dep}$.

5.3 Comparison with the PHZ

The *Planck* science team compiled a list of 2151 high-redshift (PHZ) source candidates with $S_{545\ \rm GHz} \geq 500$ mJy in the cleanest 26 per cent of the sky using a component-separation procedure applied to the *Planck* and *IRAS* data (Planck Collaboration XXXIX 2016). Rather than starting from the compact source catalogues PCCS1 or PCCS2, the PHZ sources are identified from the analysis of the *Planck* survey data itself. Therefore, the PHZ selection diverges from our approach from this starting point. The stated intent of the PHZ selection is 'to select the most luminous cold submillimetre sources with SEDs peaking between 353 and 857 GHz at 5 arcmin resolution'. However, the details of the colour selections are also substantially different from ours (Section 2.1), and the readers are referred to the PHZ paper for the details of their candidate selection. Their final list of 2151 PHZ source candidates is an order of magnitude larger in size compared with our final candidate list covering nearly the same area (see Section 2 and Table 1). The PHZ catalogue is substantially different from the PCCS catalogues, and this is an important factor to consider for this comparison with our sample (see below).

The source density of the PHZ catalogue, $\sim$0.2 per deg^{-2}, is much higher than the known source density of the submillimetre and IR source populations at the sample flux density level ($\geq$500 mJy at 545 GHz), and the Planck collaboration has suggested that the majority of these PHZ sources with estimated IR luminosity of $L_{\rm IR} = (0.5-7) \times 10^{14}$ $L_{\odot}$ are actually blends of multiple objects, rather than single strongly lensed objects. By analysing the *Herschel* follow-up observations of the 228 *Planck* high-z source candidates (Planck Collaboration XXVII 2015), the Planck collaboration estimates that 3 per cent of the PHZ sources are strongly lensed DSFGs at $z = 2$–4 while the remaining sources are overdensities consisting of 10 or more closely clustered DSFGs. Martinache et al. (2018) have reported a significant overdensity of *Spitzer*/IRAC sources associated with 82 PHZ protocluster candidates identified by the *Herschel* data, and detailed studies of a few individual PHZ sources have demonstrated an overdensity in the redshift space as well (Flores-Cacho et al. 2016; Kneissl et al. 2019; Koyama et al. 2021). However, based on a statistical analysis and modelling, Negrello et al. (2017) have argued that the majority of these PHZ sources are positive Poisson fluctuations of the number of dusty sources within the *Planck* beam, rather than being individual clumps of physically bound galaxies.

When we first started our high-redshift source search in the *Planck* database in 2013, we were unaware that the *Planck* collaboration science team was conducting its own search for high-redshift galaxies in the full survey data. The idea of candidate selection by analysing SED and colour selection is broadly similar, but the differences in the parent *Planck* catalogues and source filtering resulted in two rather different final catalogues of high-redshift source candidates. Examining these details should yield an interesting insight into the nature of these candidate sources.

Comparisons of the 857–545 GHz and 545–353 GHz flux density and flux density ratios, shown in Fig. 15, clearly demonstrate how the two samples differ in their sample definitions. The comparison of the $S_{857\ \rm GHz}/S_{545\ \rm GHz}$ flux density ratio as a function of 857 GHz flux density (left-hand panel) shows that the overlap between the PHZ sample (small dots) and our confirmed high-redshift DSFGs (large dots) is not very good. This is consistent with our finding only five (PJ020941.3, PJ084650.1, PJ113921.7, PJ144958.6, and PJ154432.4) of our 27 PCCS-selected $z \geq 1$ DSFGs (from this study and Harrington et al. 2016) with a counterpart within a 150 arcsec search radius in the PHZ catalogue. This figure demonstrates that the exclusion of the majority of our sources in the PHZ catalogue is the direct consequence of the colour and flux cuts used by the PHZ catalogue generation: (i) $S_{857\ \rm GHz}/S_{545\ \rm GHz} < 2$, and (ii) and $S_{545\ \rm GHz} > 500$ mJy (see Planck Collaboration XXXIX 2016). The combined effect of these two selection criteria leads to a fan-shaped distribution of PHZ sources on the left-hand panel, and *both* of these selection filters play a role in excluding the majority of our PCCS-selected high-redshift DSFGs. Among the sources detected in both 545 and 353 GHz bands, the overlap is much better as seen on the right-hand panel. Unlike the first case, the flux density cut of $S_{545\ \rm GHz} > 500$ mJy has only a minor impact here, presumably because the dust peak shifts into the *Planck* 545 GHz band at $z \geq 2$.

As noted by the PHZ team in their paper, the overlap between the PHZ and PCCS catalogues is extremely small, with a total of only 35 sources in common. The number of 857 GHz drop-out sources in the PCCS catalogues is also very small ($\sim$100 total, see Section 2.1), and the filtering for 'cold' SED sources adopted for the PHZ catalogue must be an important factor behind this discrepancy between the PCCS and the PHZ catalogues. To be clear, the PHZ catalogue sources are not exclusively 857 GHz drop-outs, as is obvious in the left-hand panel of Fig. 15. However, the PHZ sample selection for cold dust colour is directly responsible for excluding the majority of the PCCS-selected PASSAGES sources.

The Planck collaboration paper also suggests that the PHZ catalogue is complementary to the PCCS catalogues by picking out the faintest and coldest objects at high latitude. However, the comparisons shown in Fig. 15 does not fully support this claim in that their $S_{857\ \rm GHz}/S_{545\ \rm GHz} < 2$ colour selection combined with the flux density cutoff of $S_{545\ \rm GHz} > 500$ mJy is the primary driver behind excluding the majority of the strongly magnified DSFGs identified by our PASSAGES project. In fact, the ranges of the 857 and 545 GHz flux density are very similar.

In summary, our filtering of the PCCS catalogues and the sample selection criteria used to identify the 'cold' dusty sources for the PHZ catalogue are similar enough that they could potentially recover the

Downloaded from https://academic.oup.com/mnras/article/515/3/3911/6603847 by guest on 28 January 2026

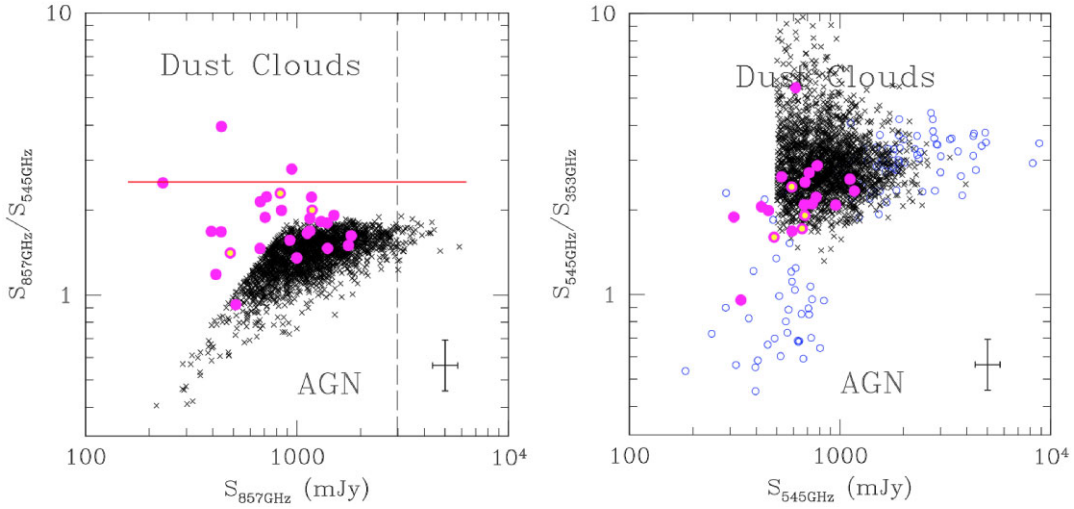

Figure 15. Plots of flux density ratios as a function flux density as in Fig. 3 but this time comparing the *Planck* PHZ sources (small black dots, Planck Collaboration XXXIX 2016). All confirmed high-redshift PCCS sources and a subsample from the *Planck-Herschel* study by Cañameras et al. (2015) are shown with large filled and empty magenta circles. As in Fig. 3, the red line on the left panel is the flux density ratio used to define our sample, and the empty blue circles on the right panel are 857 GHz dropout sources which are either very cold dust sources or flat spectrum AGNs. Typical uncertainties are shown on the bottom-right corner of each figure.

same objects, but they actually do not. The comparison of the two catalogues in Fig. 15 shows that important detailed differences in the PHZ sample definition are leading to the exclusion of the majority of the strongly lensed DSFGs we identified from the PCCS catalogues in the PHZ catalogue. It will be interesting to see whether future searches for strong lensed DSFGs in the PHZ catalogue turns up a different population of colder dust sources compared with those found by the PASSAGES project.

6 CONCLUSIONS

We report the identification of 22 high-redshift luminous DSFGs from a candidate list constructed using the PCCS (Planck Collaboration XXVIII 2014) and a carefully designed colour and magnitude selection algorithm that utilizes the all-sky *Planck* and *WISE* photometry data. Their redshifts of $z = 1.1$–3.3 are confirmed through AzTEC 1.1 mm continuum imaging and CO spectroscopy obtained using the RSR on the *LMT*. Combined with the eight high-redshift *Planck* sources identified using the archival *Herschel* data in our pilot study (Harrington et al. 2016), this study increases the total number of high-redshift sources drawn from the PCCS to 30. Our ALMA 1.1 mm continuum imaging and photometry show that all 12 *Planck* sources observed at $\theta \sim 0.4$ arcsec resolution are strongly lensed with characteristic ring or arc morphology. Two of the PCCS sources are shown to be $z \approx 0.2$ ULIRGs, and the three pairs of sources found in the directions of massive foreground clusters appear to be multiple images of the same object or associated objects based on their common CO redshifts.

The apparent IR luminosity of the $z \geq 1$ *Planck*-selected DSFGs identified in our PASSAGES project ranges between 0.1 and 3.1 times 10^{14} $L_\odot$ with a median value of 1.2×10^{14} $L_\odot$, making them some of the most luminous galaxies ever known. The *Planck*-selected DSFGs from this study, along with those from our pilot study by Harrington et al. (2016) and those similarly identified by Cañameras et al. (2015), account for 17 out of 25 (68 per cent) of *all* known objects with $L_{IR} \geq 10^{14}$ $L_\odot$. In addition, the five *Planck*-selected DSFGs with $L_{IR} \geq 10^{13}$ $L_\odot$ at $z < 2$ are also some of the most luminous objects found in this redshift range. Their molecular gas mass M_{H2} derived from the measured CO line luminosity ranges between 0.7 and 9.3 times $10^{12}M_\odot$, uncorrected for their unknown lensing magnification, and they are in a good agreement with the cold ISM mass M_{ISM} derived from the 1 mm continuum photometry. Correcting for their mean magnification of $\mu \approx 10$, their luminosity and gas masses are similar to those of the most luminous SMGs discovered by millimetre and submillimetre surveys of the cosmology deep fields, suggesting these *Planck*-selected DSFGs are the magnified versions of the most luminous DSFGs found at the same redshifts. Their gas depletion times τ_{dep} ($\equiv M_{H2}/SFR$) range between 100 and 500 Myr, the same as those of the unlensed DSFGs and star-forming MS galaxies studied by Magnelli et al. (2012), Magdis et al. (2012), and Tacconi et al. (2013). This common SF efficiency independent of luminosity and galaxy mass further supports the idea that the underlying SF process is dictated by the internal structure of the GMCs, rather than global galaxy properties (Scoville et al. 2017).

An interesting outcome from the analysis of the SEDs of these extremely luminous *Planck*-selected DSFGs is the absence of any detectable AGN activity, unlike the HyLIRGs discovered by other all-sky IR surveys done by *IRAS* and *WISE*. Growth of SMBH concurrent with a triggered starburst during the period of high gas mass accretion has been proposed by Sanders et al. (1988) based on the high frequency of warm IR sources among the most luminous ULIRGs in the local universe, and nearly simultaneous growth of SMBH and associated luminous AGN activity is one of the key predictions for a rapid galaxy growth driven by a gas-rich merger (Hopkins et al. 2006, 2008). In contrast to this popular scenario, both the SED analysis of individual galaxies shown in Fig. 9 and the mid-IR to FIR colour diagnostic analysis shown in Fig. 11 suggest that the nearly entire luminosity of these *Planck* sources is powered by SF alone, in line with the mid-IR and X-ray studies that have found detectable AGN activities in less than 20–30 per cent of high-redshift DSFGs (see review by Casey et al. 2014). A gas column density exceeding $10^{24–25}$ cm^{-2} can obscure any AGN activity even in the IR, but the gas and dust has to cover both the AGN activity and any structures cleared by associated feedback process, with little

Downloaded from https://academic.oup.com/mnras/article/515/3/3911/6603847 by guest on 28 January 2026

room for any clumpy geometry. Future IR ($\lambda_{rest} = 30-100\,\mu m$) and hard X-ray (>30–100 keV) observations are crucial for setting strong constraints on any energetic contribution by deeply embedded AGN activity.

Lastly, the comparison of our sample with the PHZ (Planck Collaboration XXXIX 2016) shows remarkably little overlap. Important differences in the PHZ sample definition are leading to the exclusion of the majority of strongly lensed DSFGs we identified from the PCCS catalogues in the PHZ catalogue. It will be interesting to see what any future follow-up studies may reveal about the nature of these PHZ sources.

Confirming whether the majority of the 118 *Planck*-selected high-redshift DSFG candidates are real is an interesting next step in the PASSAGES project. A much larger sample of *Planck*-selected DSFGs can offer a potentially important insight into the nature of the submillimetre and FIR source populations and the effects of gravitational lensing with significantly improved statistics. Obtaining a larger sample can also offer more interesting constraints on the growth of SMBHs among galaxies with the highest intrinsic SFR. Gravitational lensing offers a rare opportunity to probe 10–100 pc spatial scales inaccessible to the current generation of astronomical facilities. Finding the best laboratories for probing physical processes that govern the rapid growth and subsequent shutoff of SF in the early epochs is also important next goal.

ACKNOWLEDGEMENTS

Authors thank N. Z. Scoville for his insightful discussions on the comparison of luminosity produced by a starburst and a SMBH. We also benefited from useful discussions with R. Snell and J. Vieira. MSY thanks D. F. Gallup for his assistance during the initial development of the project and J. L. Yun for producing some of the plots shown here. This work would not have been possible without the long-term financial support from the Mexican Science and Technology Funding Agency, CONACYT (Consejo Nacional de Ciencia y Tecnología) during the construction and early operational phase of the *Large Millimeter Telescope Alfonso Serrano*, as well as support from the US National Science Foundation via the University Radio Observatory programme, the Instituto Nacional de Astrofísica, Óptica y Electrónica (INAOE) and the University of Massachusetts, Amherst (UMass). The UMass *LMT* group acknowledges support from NSF URO and ATI grants (AST-0096854, AST-0215916, AST-0540852, and AST-0704966) for the *LMT* project and the construction of the RSR and AzTEC. AM thanks support from Consejo Nacional de Ciencia y Tecnología (CONACYT) project A1-S-45680. DB, KH, and RC would like to acknowledge support from a William Bannick Student Travel Grant. We are grateful to all of the *LMT* observers from Mexico and UMass who took data for this project. This publication makes use of data products from the Wide-field Infrared Survey Explorer, which is a joint project of the University of California, Los Angeles, and the Jet Propulsion Laboratory/California Institute of Technology, funded by the National Aeronautics and Space Administration. This work is based in part on observations made with the *Herschel Space Observatory*, which is an *ESA Space Observatory* with science instruments provided by European-led Principal Investigator consortia and with important participation from NASA, and the *Planck*, which is a European Space Agency mission with significant NASA involvement. This research has made use of the NASA/ IPAC Extragalactic Database (NED) which is operated by the Jet Propulsion Laboratory, California Institute of Technology, under contract with the National Aeronautics and Space Administration. This research has made use of the NASA/IPAC Infrared Science Archive, which is funded by the National Aeronautics and Space Administration and operated by the California Institute of Technology. This paper makes use of the following ALMA data: ADS/JAO.ALMA#2017.1.01214.S. ALMA is a partnership of ESO (representing its member states), NSF (USA), and NINS (Japan), together with NRC (Canada), MOST and ASIAA (Taiwan), and KASI (Republic of Korea), in cooperation with the Republic of Chile. The Joint ALMA Observatory is operated by ESO, AUI/NRAO, and NAOJ. The National Radio Astronomy Observatory is a facility of the National Science Foundation operated under cooperative agreement by Associated Universities, Inc.

DATA AVAILABILITY

The data underlying this article are available in the article and in its online supplementary material. Other data sets were derived from sources in the public domain, such as the ALMA and *HST* data archives as well as NASA/IPAC IRSA.

REFERENCES

Amodeo S. et al., 2018, ApJ, 853, 36
Amvrosiadis A. et al., 2018, MNRAS, 475, 4939
Assef R. J. et al., 2015, ApJ, 804, 27
Bakx T. J. L. C. et al., 2018, MNRAS, 473, 1751
Barvainis R., Antonucci R., Coleman P., 1992, ApJ, 399, L19
Becker R. H., White R. L., Helfand D. J., 1995, ApJ, 450, 559
Beckwith S. V. W. et al., 2006, AJ, 132, 1729
Béthermin M., De Breuck C., Sargent M., Daddi E., 2015, A&A, 576, L9
Blain A. W., 1998a, MNRAS, 295, 92
Blain A. W., 1998b, MNRAS, 297, 511
Blain A. W., Smail I., Ivison R. J., Kneib J.-P., Frayer D. T., 2002, Phys. Rep., 369, 111
Bolatto A. D., Wolfire M., Leroy A. K., 2013, ARA&A, 51, 207
Bussmann R. S. et al., 2013, ApJ, 779, 25
Bussmann R. S. et al., 2015, ApJ, 812, 43
Cañameras R. et al., 2015, A&A, 581, A105
Cañameras R. et al., 2018, A&A, 620, A61
Carilli C. L., Walter F., 2013, ARA&A, 51, 105
Carlstrom J. E. et al., 2011, PASP, 123, 568
Casey C. M., Narayanan D., Cooray A., 2014, Phys. Rep., 541, 45
Casey C. M. et al., 2018, ApJ, 862, 77
Cen R., Ostriker J. P., 1999, ApJ, 519, L109
Chung A., Narayanan G., Yun M. S., Heyer M., Erickson N. R., 2009, AJ, 138, 858
Clements D. L. et al., 2014, MNRAS, 439, 1193
Clements D. L. et al., 2016, MNRAS, 461, 1719
Condon J. J., 1992, ARA&A, 30, 575
Condon J. J., Cotton W. D., Greisen E. W., Yin Q. F., Perley R. A., Taylor G. B., Broderick J. J., 1998, AJ, 115, 1693
Coppin K. E. K. et al., 2007, ApJ, 665, 936
Dannerbauer H., Harrington K., Díaz-Sánchez A., Iglesias-Groth S., Rebolo R., Genova-Santos R. T., Krips M., 2019, AJ, 158, 34
Deshmukh S. et al., 2018, ApJ, 864, 166
Díaz-Sánchez A., Iglesias-Groth S., Rebolo R., Dannerbauer H., 2017, ApJ, 843, L22
Draine B. T., 1989, in Böhm-Vitense E., ed., Proc. 22nd Eslab Symp., Infrared Spectroscopy in Astronomy. European Space Agency, p. 93
Dye S. et al., 2015, MNRAS, 452, 2258
Dye S. et al., 2018, MNRAS, 476, 4383
Eales S. et al., 2010, PASP, 122, 499
Efstathiou A., Rowan-Robinson M., Siebenmorgen R., 2000, MNRAS, 313, 734
Enia A. et al., 2018, MNRAS, 475, 3467
Erickson N., Narayanan G., Goeller R., Grosslein R., 2007, in Baker A. J., Glenn J., Harris A. I., Mangum J. G., Yun M. S., eds, ASP Conf. Ser.

Downloaded from https://academic.oup.com/mnras/article/515/3/3911/6603847 by guest on 28 January 2026

Vol. 375, From Z-Machines to ALMA: (Sub)Millimeter Spectroscopy of Galaxies. Astron. Soc. Pac., San Francisco, p. 71
Flores-Cacho I. et al., 2016, A&A, 585, A54
Fowler J. W. et al., 2007, Appl. Opt., 46, 3444
Frye B. L. et al., 2019, ApJ, 871, 51
Geach J. E. et al., 2015, MNRAS, 452, 502
González-Nuevo J. et al., 2012, ApJ, 749, 65
Gralla M. B. et al., 2020, ApJ, 893, 104
Greve T. R. et al., 2012, ApJ, 756, 101
Harrington K. C. et al., 2016, MNRAS, 458, 4383
Harrington K. C. et al., 2021, ApJ, 908, 95
Herranz D. et al., 2013, A&A, 549, A31
Hezaveh Y. D., Holder G. P., 2011, ApJ, 734, 52
Hopkins P. F., Hernquist L., Cox T. J., Di Matteo T., Robertson B., Springel V., 2006, ApJS, 163, 1
Hopkins P. F., Hernquist L., Cox T. J., Kereš D., 2008, ApJS, 175, 356
Hughes D. H. et al., 2020, in Marshall H. K., Spyromilio J., Usuda T., eds, Proc. SPIE Conf. Ser. Vol. 11445, Ground-based and Airborne Telescopes VIII. SPIE, Bellingham, p. 1144522
Iglesias-Groth S., Díaz-Sánchez A., Rebolo R., Dannerbauer H., 2017, MNRAS, 467, 330
Iono D. et al., 2016, ApJ, 829, L10
Irwin M. J., Ibata R. A., Lewis G. F., Totten E. J., 1998, ApJ, 505, 529
Ivison R. J., Smail I., Papadopoulos P. P., Wold I., Richard J., Swinbank A. M., Kneib J. P., Owen F. N., 2010, MNRAS, 404, 198
Kennicutt R. C., Jr, 1998, ARA&A, 36, 189
Keres D., Katz N., Weinberg D. H., Davé R., 2005, MNRAS, 363, 2
Khatri R., 2016, A&A, 592, A48
Kirkpatrick A. et al., 2012, ApJ, 759, 139
Kirkpatrick A. et al., 2013, ApJ, 763, 123
Kirkpatrick A., Sharon C., Keller E., Pope A., 2019, ApJ, 879, 41
Kneissl R. et al., 2019, A&A, 625, A96
Kormendy J., Ho L. C., 2013, ARA&A, 51, 511
Koyama Y. et al., 2021, MNRAS, 503, L1
Madau P., Dickinson M., 2014, ARA&A, 52, 415
Magdis G. E. et al., 2012, ApJ, 760, 6
Magnelli B. et al., 2012, A&A, 539, A155
Marsden D. et al., 2014, MNRAS, 439, 1556
Martinache C. et al., 2018, A&A, 620, A198
Massardi M. et al., 2018, A&A, 610, A53
Negrello M., Perrotta F., González-Nuevo J., Silva L., de Zotti G., Granato G. L., Baccigalupi C., Danese L., 2007, MNRAS, 377, 1557
Negrello M. et al., 2010, Science, 330, 800
Negrello M. et al., 2017, MNRAS, 470, 2253
Nesvadba N. P. H., Cañameras R., Kneissl R., Koenig S., Yang C., Le Floc'h E., Omont A., Scott D., 2019, A&A, 624, A23
Oliver S. J. et al., 2012, MNRAS, 424, 1614
Penney J. I. et al., 2020, MNRAS, 496, 1565
Perera T. A. et al., 2008, MNRAS, 391, 1227
Planck Collaboration VII, 2013, A&A, 550, A133
Planck Collaboration XI, 2014, A&A, 571, A11
Planck Collaboration XXVIII, 2014, A&A, 571, A28
Planck Collaboration XXVII, 2015, A&A, 582, A30
Planck Collaboration XXVI, 2016, A&A, 594, A26
Planck Collaboration XXXIX, 2016, A&A, 596, A100
Planck Collaboration LV, 2020, A&A, 644, A99
Polletta M. et al., 2007, ApJ, 663, 81
Reuter C. et al., 2020, ApJ, 902, 78
Rowan-Robinson M., 2000, MNRAS, 316, 885
Rowan-Robinson M. et al., 1991, Nature, 351, 719
Rybak M., McKean J. P., Vegetti S., Andreani P., White S. D. M., 2015, MNRAS, 451, L40
Sanders D. B., Mirabel I. F., 1996, ARA&A, 34, 749
Sanders D. B., Soifer B. T., Elias J. H., Neugebauer G., Matthews K., 1988, ApJ, 328, L35
Schinnerer E. et al., 2019, ApJ, 887, 49
Scott K. S. et al., 2008, MNRAS, 385, 2225
Scoville N., Young J. S., 1983, ApJ, 265, 148
Scoville N. et al., 2016, ApJ, 820, 83
Scoville N. et al., 2017, ApJ, 837, 150
Smail I. et al., 2007, ApJ, 654, L33
Smail I. et al., 2021, MNRAS, 502, 3426
Solomon P. M., Downes D., Radford S. J. E., Barrett J. W., 1997, ApJ, 478, 144
Spilker J. S. et al., 2016, ApJ, 826, 112
Strandet M. L. et al., 2016, ApJ, 822, 80
Strauss M. A., Huchra J. P., Davis M., Yahil A., Fisher K. B., Tonry J., 1992, ApJS, 83, 29
Su T. et al., 2017, MNRAS, 464, 968
Swinbank A. M. et al., 2010, Nature, 464, 733
Tacconi L. J. et al., 2013, ApJ, 768, 74
Tacconi L. J., Genzel R., Sternberg A., 2020, ARA&A, 58, 157
Tadaki K. et al., 2018, Nature, 560, 613
Teng S. H. et al., 2009, ApJ, 691, 261
Thompson T. A., Quataert E., Murray N., 2005, ApJ, 630, 167
Treister E., Urry C. M., Schawinski K., Cardamone C. N., Sanders D. B., 2010, ApJ, 722, L238
Trombetti T., Burigana C., Bonato M., Herranz D., De Zotti G., Negrello M., Galluzzi V., Massardi M., 2021, A&A, 653, A151
Tsai C.-W. et al., 2015, ApJ, 805, 90
Vieira J. D. et al., 2010, ApJ, 719, 763
Vieira J. D. et al., 2013, Nature, 495, 344
Viero M. P. et al., 2014, ApJS, 210, 22
Walter F. et al., 2014, ApJ, 782, 79
Wang W.-H., Barger A. J., Cowie L. L., 2009, ApJ, 690, 319
Wang W.-H. et al., 2016, ApJ, 833, 195
Wardlow J. L. et al., 2013, ApJ, 762, 59
Weiß A., Downes D., Neri R., Walter F., Henkel C., Wilner D. J., Wagg J., Wiklind T., 2007, A&A, 467, 955
Weiß A. et al., 2013, ApJ, 767, 88
Wen Z. L., Han J. L., 2015, ApJ, 807, 178
Whitaker K. E., Pope A., Cybulski R., Casey C. M., Popping G., Yun M. S., 2017, ApJ, 850, 208
Wilson G. W. et al., 2008, MNRAS, 386, 807
Wright E. L. et al., 2010, AJ, 140, 1868
Wu J. et al., 2018, ApJ, 852, 96
Yamaguchi Y. et al., 2019, ApJ, 878, 73
Yang C. et al., 2017, A&A, 608, A144
Yun M. S., Carilli C. L., 2002, ApJ, 568, 88
Yun M. S., Reddy N. A., Condon J. J., 2001, ApJ, 554, 803
Yun M. S. et al., 2008, MNRAS, 389, 333
Yun M. et al., 2009, in Astro2010: The Astronomy and Astrophysics Decadal Survey, Science White Papers, no. 330
Yun M. S. et al., 2012, MNRAS, 420, 957
Yun M. S. et al., 2015, MNRAS, 454, 3485
Yun M. S., Schloerb F. P., Narayanan G., Erickson N., 2020, LMT Memo
Zavala J. A. et al., 2021, ApJ, 909, 165

APPENDIX A: PHOTOMETRY OF CANDIDATE SOURCES UNDETECTED BY AZTEC

AzTEC follow-up observations of the 30 sources identified by the *Planck–WISE* selection are described in Section 3.1. The 13 sources clearly detected as bright 1.1 mm continuum sources are summarized in Table 3. The remaining 17 sources are undetected by AzTEC, and the details of those observations and their sensitivity are summarized in Table A1. These initial targets for AzTEC observations were drawn from a much larger parent list than our 'high priority' candidates. There are no obvious indications in the *Planck* data that would set these non-detections apart from the detected sources. At least some of these non-detections appear to be compact Galactic cirrus clouds that passed through our initial colour–magnitude filters, as our strategy was all along to keep the initial filtering simple and to identify high-

Downloaded from https://academic.oup.com/mnras/article/515/3/3911/6603847 by guest on 28 January 2026

Table A1. Summary of sources undetected by AzTEC on *LMT*.

Source ID	RA (J2000)	DEC (J2000)	AzTEC Dates	AzTEC Int. time (min)	$S_{1100\mu}$[a]
PJ012508.1	01h25m08^{s}.1	+29d22m55s	2015-02-05	10	≤7.8 mJy
PJ042847.0	04h28m47^{s}.0	−27d30m58s	2016-01-24	10	≤6.7 mJy
PJ082721.1	08h27m21^{s}.1	+60d16m08s	2015-04-06	10	≤4.2 mJy
PJ083622.6	08h36m22^{s}.6	+23d40m18s	2016-01-22	10	≤7.1 mJy
PJ084759.7	08h47m59^{s}.7	+17d42m12s	2014-11-10	10	≤3.2 mJy
PJ091626.2	09h16m26^{s}.2	+18d55m35s	2015-04-05	10	≤3.9 mJy
PJ093055.1	09h30m55^{s}.1	+46d48m57s	2015-04-05, 2015-04-06	20	≤3.3 mJy
PJ094609.1	09h46m09^{s}.1	+00d43m12s	2016-01-23	10	≤8.6 mJy
PJ094921.3	09h49m21^{s}.3	+14d50m28s	2016-01-22	10	≤7.9 mJy
PJ095326.1	09h53m26^{s}.1	+70d53m40s	2016-01-24	10	≤7.1 mJy
PJ100023.1	10h00m23^{s}.1	+12d15m21s	2015-04-06	10	≤4.1 mJy
PJ101804.5	10h18m04^{s}.5	+28d12m05s	2016-02-05	10	≤9.3 mJy
PJ103146.9	10h31m46^{s}.9	−22d12m44s	2015-02-24	10	≤4.0 mJy
PJ105248.6	10h52m48^{s}.9	+42d15m43s	2015-02-24	10	≤4.2 mJy
PJ112025.4	11h20m25^{s}.4	+05d53m33s	2016-02-05	10	≤5.8 mJy
PJ112716.7	11h27m16^{s}.7	+42d28m39s	2016-01-23	10	≤7.9 mJy
PJ114329.5	11h43m29^{s}.5	+68d01m07s	2016-01-23	10	≤6.8 mJy

Note.
[a]$S_{1100\mu}$ listed is a 3σ upper limit based on the photometry over a 1.5 arcmin diameter region centred on the source position.

redshift sources using *LMT* follow-up observations (see discussions in Section 2).

APPENDIX B: NOTES ON INDIVIDUAL SOURCES

In this section we briefly summarize each of the 13 high-redshift *Planck* sources which have not been studied previously (Table 3). Complementing the eight sources identified in Harrington et al. (2016), there are 24 additional high-redshift *Planck* sources identified with the selection criteria presented in this study.

P011646.8: The derived source redshift, $z = 2.125$, is based on the CO (3–2) line detected with the RSR and subsequent spectroscopic confirmation by Harrington et al. (2021). This source is detected in two *Planck* bands and is also imaged in 260 GHz continuum using ALMA. The *HST*/WFC3 1.6 μm image reveals a ∼6 arcsec diameter, nearly complete double-Einstein ring. No redshift information is available for the lensing galaxy at the moment. The ALMA 260 GHz image spatially resolves the two dominant lensing arc features in dust continuum.

PJ014341.2: A photometric redshift support from the combined SED analysis of the *Planck*, *Herschel*, and ALMA measurements suggests that the single line detected by the RSR measurement corresponds to a CO (2–1) line emission at a source redshift, $z = 1.095$. The ALMA 260 GHz observation reveals a compact galaxy–galaxy lensing system with a partially complete Einstein ring with a diameter of ∼1.5 arcsec. The foreground lensing SDSS galaxy has a spectroscopic redshift of $z = 0.594$.

PJ022634.0: With a *Planck* detection of $S_{350} \sim 1800$ mJy, this system is the brightest in our sample. Its apparent SED peaking in the *Planck* 350 μm band suggests this to be a low redshift ($z \leq 2$) source, but our subsequent spectroscopic follow-up observations by Harrington et al. (2021) have shown that the single line detected by the RSR is a CO (3–2) line at $z = 3.120$. The *HST*/WFC3 1.6 μm image (Lowenthal et al., in preparation) shows an Einstein ring with a diameter of ∼3 arcsec centred on a large elliptical galaxy with a photometric redshift of $z = 0.41$ (Wen & Han 2015).

PJ030510.6: The derived source redshift, $z = 2.263$, is based on the CO (3–2) line detection with the RSR, and this is confirmed by our follow-up spectroscopy (Harrington et al. 2021). It is detected in two *Planck* bands, and ALMA 260 GHz measurements recover the total flux density measured by AzTEC 1.1 mm observations. The ALMA resolves the source into two separate and compact peaks with a less than 1 arcsec separation. The *HST*/WFC3 1.6 μm image shows one stellar component well centred on the brighter 260 GHz peak while the second stellar component is clearly offset from the second 260 GHz peak. No redshift is available for either stellar galaxies.

PJ074851.7 and PJ074852.6: This cluster lensed system at $z = 2.755$ has two *WISE*-selected candidates, PJ074851.7 and PJ074852.6. The two colour-selected *WISE* sources are targeted separately using the RSR, and a CO (3–2) line is detected in both objects with a redshift of $z = 2.755$. These two sources are seen as a single *Planck* source, with $S_{350} \sim 1000$ mJy. The *HST*/WFC3 1.6 μm image shows several lensed arc features in a cluster field, and one of the lensed arclets extends 15–20 arcsec in length. The source redshift of PJ074852.6 has been verified with our follow-up spectroscopy campaign (Harrington et al. 2021). The foreground cluster PSZ2 G157.43+30.34 has a published redshift of 0.42 by Khatri (2016) and 0.402 by Amodeo et al. (2018).

PJ084648.6 and PJ084650.1: This cluster lensed system at $z = 2.66$ has two *WISE*-selected candidates, PJ084648.6 and PJ084650.1, and they are both detected in CO (3–2) line by the RSR at $z = 2.664$ and $z = 2.661$, respectively. The *HST*/WFC3 1.6 μm image as well as ALMA 260 GHz continuum image show them to be two distinct lensed arcs. Because they are both associated with the same *Planck* point source ($S_{350} \sim 1750$ mJy), they are treated as a single *Planck* source in this paper. The source redshift of PJ084650.1 has been verified with our subsequent spectroscopic follow-up observations by Harrington et al. (2021). The redshift of the foreground cluster is somewhat uncertain since few spectroscopic redshifts are available in this field. The bright elliptical galaxy located between the two lensed arcs is an SDSS source with a photometric redshift of $z \sim 0.4$.

PJ105322.6: The two CO lines detected in the RSR spectrum leads to an unambiguous redshift of $z = 3.549$ for this 857 GHz drop-out *Planck* source. This is the brightest 1.1 mm sources detected

Downloaded from https://academic.oup.com/mnras/article/515/3/3911/6603847 by guest on 28 January 2026

with AzTEC (202 ± 30 mJy) and has a fully mapped rest frame FIR SED because this is one of the *Planck* sources studied using *Herschel* (PLCK_G145.2+50.9). The Submillimeter Array (SMA) 850 μm continuum imaging by Cañameras et al. (2015) shows a nearly complete Einstein ring with ∼5 arcsec radius. Using their *HST* F110W and F160W band imaging and ground-based spectroscopy, Frye et al. (2019) have shown that the lensing mass is a small compact group of red galaxies at $z = 0.837$.

PJ112713.4: This system has only a single *Planck* detection, with $S_{350} \sim 200$ mJy, and was not observed by AzTEC or by ALMA. The single line detected by the RSR observations is tentatively interpreted as a CO (2–1) line at $z = 1.303$, and this is later confirmed by our spectroscopic follow-up observations (Harrington et al. 2021). The *HST*/WFC3 1.6 μm image shows an Einstein ring with ∼1 arcsec diameter centred on a compact galaxy with an SDSS photometric redshift of $z = 0.42$, suggesting a galaxy–galaxy lensing (Lowenthal et al., in preparation).

PJ113805.5: The single line detected by the RSR is interpreted to be a CO (2–1) line at a redshift of $z = 2.019$ based on photometric support using the SED analysis, and this redshift is confirmed by our spectroscopic follow-up observations (Harrington et al. 2021). This source is detected in all three *Planck* bands and by ALMA, with $S_{350} \sim 200$ mJy. It is likely lensed by a single foreground elliptical galaxy with an SDSS photometric redshift of $z = 0.52$, as the ALMA 260 GHz continuum image shows a compact (≤1.5 arcsec) elongated structure centred on the optical galaxy seen in the *HST*/WFC3 1.6 μm image.

PJ113921.7: PJ113921.7 is another high-redshift *Planck* source studied with a *Herschel* follow-up study (PLCK_G231.3+72.2) that we independently recovered from the PCCS using our *WISE* colour selection and AzTEC photometry. The CO (3–2) line redshift of $z = 2.858$ is derived from our RSR observations and the photometric support, and this redshift agrees well with those measured by other multiline studies (Cañameras et al. 2018; Nesvadba et al. 2019; Harrington et al. 2021). Our ALMA 260 GHz continuum image shows a compact ring of emission with ∼1.5 arcsec diameter, centred around a compact galaxy seen in our *HST*/WFC3 1.6 μm image (Lowenthal et al., in preparation). No visible counterpart to the ALMA 260 GHz continuum emission is seen in the *HST* image, and the redshift of the lensing galaxy is unknown.

PJ114038.5: The colour-selected *WISE* source J114038.5+53215 associated with this PCCS object shows a compact red core surrounded by a blue irregular structure, characteristic of a recent merger system in the SDSS images. It was previously identified as one of the IR bright galaxies found by the *IRAS* ('*IRAS* 2Jy Sample'), with a redshift of $z = 0.092$ (Strauss et al. 1992). The SDSS data base offers no spectroscopic data, but it reports a photometric redshift of 0.127 ± 0.029. Our RSR spectrum shows a single emission line at 98.932 GHz, and this corresponds to a spectroscopic redshift of $z = 0.1652 \pm 0.0001$ if the line is interpreted as that of CO (1–0) transition. While these redshifts do not match exactly, they are in a reasonable agreement. Considering its identification as an *IRAS* 2Jy Sample source along with its relatively bright radio continuum (16.8 ± 0.3 mJy at 1.4 GHz in the FIRST data base), we conclude that PJ114038.5 is a low-z galaxy at $z = 0.1652$.

PJ114329.5: The colour-selected *WISE* source J114329.5+680107 associated with this PCCS object is associated with a well-resolved SDSS galaxy with red colour and a smooth morphology. The SDSS spectrum shows strong emission lines and bright continuum, typical of a SFG at $z = 0.212$. Our RSR spectrum shows a single emission line at 95.124 GHz, and this corresponds to a spectroscopic redshift of $z = 0.2118 \pm 0.0001$ assuming the line is that of CO (1–0) transition. Therefore, we conclude that PJ114329.5 is another example of a foreground low-z galaxy.

PJ132217.5: The single CO (2–1) line detected with the RSR yields a redshift of $z = 2.068$ with the photometric redshift support, and this is confirmed by our spectroscopic follow-up observations (Harrington et al. 2021). The unresolved *Planck* detection peaks at $S_{350} \sim 700$ mJy, and the 260 GHz continuum is resolved into multiple clumps with the 0.4 arcsec resolution ALMA image. The lensed source morphology detected by ALMA (also a stellar Einstein ring detected in the *HST*/WFC3 1.6 μm image) is nearly 20 arcsec in diameter, and some of the 260 GHz flux might have been resolved out by ALMA, given its large angular extent. Multiple foreground galaxies are seen in the *HST*/WFC3 image, and a group potential might be responsible for the lensing (Lowenthal et al., in preparation). No spectroscopic redshifts are available for the foreground galaxies, and the brightest SDSS galaxy inside the Einstein ring has a photometric redshift of $z \sim 0.53$.

PJ132630.3: PJ132630.3 is a *Planck* high-redshift candidate source that is found in the H-ATLAS survey area, and it is one of the faintest *Planck* sources detected in just two bands, with $S_{350} \sim 300$ mJy. The single CO (3–2) line detected with the RSR yields a redshift of $z = 2.951$ with the photometric redshift support, and this redshift is confirmed by subsequent multiline observations (Yang et al. 2017; Harrington et al. 2021). This source is also identified as one of the brightest *Herschel* source found in the H-ATLAS survey with the same redshift, and Bussmann et al. (2013) derived a lensing model using their SMA 340 GHz continuum image and the lensing galaxy redshift of 0.786, with a derived magnification factor of $\mu = 4.1 \pm 0.3$ for the 340 GHz continuum. Our higher resolution ALMA 260 GHz image shows a similar morphology as their SMA 340 GHz image, which is two images straddling the central lensing galaxy.

PJ132934.2 and PJ132935.3: PJ132934.2 and PJ132935.3 are two *WISE*-selected high-redshift *Planck* candidates, associated with a single *Planck* source detected in all three *Planck* bands. The two colour-selected *WISE* sources are targeted separately using the RSR, and a CO (2–1) line is detected in both objects with a redshift of $z = 2.040$. Our ALMA 260 GHz continuum image shows that PJ132934.2 is significantly brighter than PJ132935.3 in submillimetre continuum, and the *HST*/WFC3 1.6 μm image shows they are both gravitationally lensed arcs associated with a massive foreground cluster. These sources were discovered independently by Díaz-Sánchez et al. (2017) who also used the *Planck* and *WISE* data ('Cosmic Eyebrow'). Their multiwavelength observations and modelling found that these two sources are the same object lensed by the foreground cluster at $z = 0.44$ (Dannerbauer et al. 2019).

PJ133634.9: The two bright CO lines detected by the RSR are CO (3–2) and CO (4–3) lines at $z = 3.254$, and this interpretation is further supported by our spectroscopic follow-up observations (Harrington et al. 2021). It is detected in all three *Planck* bands and by AzTEC, with $S_{350} \sim 650$ mJy. The *HST*/WFC3 1.6 μm image reveals a pair of compact galaxies with an SDSS photometric redshift of $z = 0.26$, surrounded by a ring of nebulosity with ∼1 arcsec diameter (Lowenthal et al., in preparation).

PJ141230.5: The two bright lines detected by the RSR are interpreted as CO (3–2) and CO (4–3) lines at $z = 3.310$, and this conclusion is further supported by the SED analysis for the measured photometry in the three *Planck* bands as well as the *WISE* and VLA/FIRST 1.4 GHz photometry (see Fig. 9). The foreground (likely lensing) SDSS galaxy has only a photometric redshift of 0.54 ± 0.07. However, a clear overdensity of similarly red galaxies is seen in the SDSS image centred on the *WISE* source position,

Downloaded from https://academic.oup.com/mnras/article/515/3/3911/6603847 by guest on 28 January 2026

including two galaxies with a SDSS spectroscopic redshift of $z = 0.588$ within a 30 arcsec radius, and there is a high likelihood that the foreground lensing source is also at $z = 0.588$.

PJ144653.2: This system has *Planck*, AzTEC, and ALMA measurements of the dust SED, with a peak *Planck* detection of $S_{350} \sim 1150$ mJy. Given its brightness in the rest-frame FIR, the single line detected by the RSR was initially thought to be a CO line at $z \approx 2$. However, our follow-up spectroscopy has shown that the RSR detection is of the CO (2–1) line at $z = 1.084$ (Harrington et al. 2021). The *HST*/WFC3 image shows a late type galaxy with an SDSS spectroscopic redshift of $z = 0.493$. The clearly resolved ALMA continuum peaks form a 2 arcsec diameter ring centred on the galaxy, suggesting a galaxy–galaxy lensing.

PJ144958.6: The RSR detected CO (3–2) line corresponds to a source redshift of $z = 2.153$, and this is confirmed by our spectroscopic follow-up observations (Harrington et al. 2021). The *Planck* detection peaks at $S_{350} \sim 700$ mJy, and the ALMA 260 GHz continuum observations have recovered the complete flux density of the AzTEC 1.1 mm measurements. The stellar light in the *HST*/WFC3 image and the ALMA 260 GHz continuum both trace the same ∼10 arcsec long lensed arc, with some notable differences – only parts of the stellar arc are associated with 260 GHz continuum. Therefore, this source is clearly spatially resolved by lensing and is likely a multiple system. A galaxy group (of unknown redshift) contributes to the foreground gravitational potential, resulting in one of the largest lens features in our sample.

PJ154432.4: PJ154432.4 is another high-redshift *Planck* source studied with a *Herschel* follow-up study (PLCK_G080.2+49.8) that we independently recovered from the PCCS using our *WISE* colour selection and AzTEC photometry. The CO (3–2) line redshift of $z = 2.5989 \pm 0.0003$ derived from our RSR observations and the photometric support agrees well with the redshift reported by Cañameras et al. (2015, '$z_{\rm source} = 2.6$'). The extension and morphology of the 1.1 mm continuum imaged by AzTEC instrument (see Fig. 5) matches the higher resolution SMA 850 μm image by Cañameras et al. and suggests lensing by a foreground potential with a mass exceeding 10^{13} $M_\odot$. The SDSS spectrum of the foreground lensing galaxy shows emission lines at $z = 0.672$ while Cañameras et al. reported a redshift of '$z_{\rm fg,\ sdss} = 0.5$' for the foreground galaxy. The wealth of photometry found in the *Planck* and *Herschel* database as well as our own AzTEC photometry define the SED nicely with a modified blackbody temperature of $41.4^{+7.0}_{-4.2}$ K (see Fig. 9 and Table 6), and the VLA/FIRST 1.4 GHz photometry is consistent with this object following the radio-FIR correlation (Condon 1992; Yun et al. 2001).

PJ231356.6: The bright line detected by the RSR is interpreted as the CO (3–2) line at $z = 2.215$, and this is confirmed by our spectroscopic follow-up (Harrington et al. 2021). It was detected in two *Planck* bands and was imaged by our ALMA 260 GHz continuum observations. PJ231356.6 is located in the *ACT* Equatorial Survey field and is identified as one of the 30 brightest DSFGs with computed deboosted flux density of $S_{148\rm GHz} = 3.2^{+1.7}_{-1.4}$ mJy, $S_{218\rm GHz} = 16.8^{+3.8}_{-4.4}$ mJy, and $S_{277\rm GHz} = 26.8^{+5.3}_{-5.3}$ mJy (Gralla et al. 2020). The *HST*/WFC3 image shows possibly multiple lensed objects, only some associated with the ALMA 260 GHz continuum, centred around a large elliptical galaxy with an SDSS spectroscopic redshift of $z = 0.560$.

This paper has been typeset from a TEX/LATEX file prepared by the author.

Downloaded from https://academic.oup.com/mnras/article/515/3/3911/6603847 by guest on 28 January 2026